

## SUPERCONDUCTING QUANTUM COMPUTING: STATUS AND PROSPECTS \*

F.K. WILHELM

*Department Physik, Center for Nanoscience, and Arnold-Sommerfeld Center for  
Theoretical Physics  
Ludwig-Maximilians-Universität  
Theresienstr. 37  
D-80333 München, Germany  
E-mail: wilhelm@theorie.physik.uni-muenchen.de*

K. SEMBA

*NTT Basic Research Laboratories, NTT Corporation,  
Atsugi, Kanagawa 243-0198 Japan  
CREST, Japan Science and Technology Agency  
4-1-8 Honcho, Kawaguchi, Saitama 332-0012, Japan  
E-mail: semba@nttbl.jp*

We review the experimental and theoretical status of superconducting quantum bits based on Josephson junctions in view of DiVincenzo's criteria.

This article takes a momentary (summer 2005) snapshot of the field of superconducting Josephson qubit. It serves on the one hand as an introduction to the general concept aimed at a broader quantum computing audience containing a guide to the more specific literature. A particular focus is given to the rather unique idea of manipulating macroscopic states quantum-coherently and the intellectual and practical challenges and implications of that work. On the other hand, we have attempted to review the most significant results of the field. Such a choice is necessarily subjective and we are probably not fully exhaustive. For exemplifying details we have typically described our own work — this is what we know best — in

---

\*dedicated to the memory of Martti Salomaa. Parts of the text are based on the Habilitationsschrift of FKW, Ludwig-Maximilians-Universität, 2004.

a way which highlights the broader ideas and should enable the reader to comprehend related work of other authors from the original literature.

### 1. Why Josephson qubits?

The way of computing as we know it in today's information-processing devices is called *classical computing*. This implies, that the binary information stored and manipulated is purely classical in nature: A bit is exclusively in one of its fundamental states 0 and 1. Computer programs are deterministic, such that (in principle) operating a program on a fixed set of data leads to the same output data every time. The enormous progress in hardware improvement follows the self-fulfilling Moore's law <sup>1</sup>, claiming that computer hardware performance will double every 18 months. Although failures of Moore's law are periodically predicted and have to occur at some time due to the laws of nature, it is by now expected to still persist for a time of 10–20 years <sup>2,3</sup>.

Quantum information, the type of information processed in a quantum computer, is radically different <sup>4,5</sup>: It uses the predictions of quantum mechanics, most notably the possibility of interfering possibilities for different values of observables at the same time, and to distribute the information on the physical state nonlocally using entangled states. These properties can be used as a computational resource. Using superpositions allows to operate an algorithm on all possible input values at the same time (massive quantum parallelism), using entangled states and measurements allows to act on all qubits (quantum bits) simultaneously.

The requirements for building a universal quantum computer have been collected very early by DiVincenzo <sup>6,7</sup>. These five criteria enjoy broad recognition and are, supplemented by two more on quantum communication, the basis for contemporary quantum computing research programs <sup>8</sup>. One has to be aware, that this standard paradigm is by no means exclusive, in fact, they are based on the circuit model of quantum computing, which does not apply to, e.g., adiabatic algorithms <sup>9</sup>.

The DiVincenzo criteria in a timely formulation require:

- (1) A scalable physical system of well-characterized qubits
- (2) The ability to initialize the state of the qubits to a simple fiducial state
- (3) Long (relative) decoherence times, much longer than the gate-operation time
- (4) A universal set of quantum gates

- (5) A qubit-specific measurement capability
- (6) The ability to interconvert stationary and flying qubits
- (7) The ability to faithfully transmit flying qubits between specified locations

This report will describe how superconducting qubits perform on these criteria.

So far, the physical implementation of quantum computing is most successful in nuclear magnetic resonance (NMR), where seven qubits have been implemented<sup>10</sup>. Remarkably, in NMR there is no “strong” measurement capability nor the option to initialize a well-defined initial state<sup>11</sup>. Another successful line of implementations comes from optical and atomic physics, such as ion traps<sup>12,13</sup>, atoms in cavities<sup>14,15</sup>, linear optics<sup>16</sup>, and neutral atoms<sup>17</sup>. All these realizations have the general idea in common, that they start out from microscopic quantum systems, systems whose quantum-mechanical properties are well-established and in principle easy to demonstrate experimentally. Consequently, the phase coherence times are very long. The experimental progress towards today’s level has been the ability to externally control these systems with high accuracy and to connect many of them to larger coupled quantum systems. However, it is still not evident whether these systems are really scalable, although a number of theoretical proposals for scalable ion trap computing have been brought forward<sup>18</sup>.

## 2. Solid-state quantum computation

Solid state circuits are readily scalable to nearly arbitrary sizes, as can be seen in the computers available today. In these computers, the information being processed is purely classical. The sheer size of a solid renders many of the quantum effects invisible, which would be visible in atomic and molecular systems. However, the physics laying the foundation of classical computers is already fundamentally quantum: The function of transistors relies on the band structure of semiconductor materials<sup>19</sup>, which is a generic quantum-mechanical effect. Remarkably, also the size of a single transistor (characterized by the gate length) is on the order of 100 nm or even below and hence does not rule out mesoscopic effects<sup>20</sup>. The same holds for the enormous clock speed of several GHz. Hence, as solid state setups are more and more miniaturized, quantum effects become important. This is the idea of mesoscopic solid-state physics<sup>21,22</sup>. Superconducting mesoscopic systems are in particular appealing, as the conduction electrons are con-

densed into a macroscopic quantum wave function already. It has already been proposed in the 80s (for SQUID systems)<sup>23,24,25,26,27</sup> and in the 90s (for Coulomb blockade devices)<sup>28,29</sup>, that collective variables such as flux and charge can be brought into superposition of two macroscopically distinct values. This enterprise has been pursued ever since, but it was only in the late 90s that it received the high degree of attention and interest it has now. This increase in interest was largely due to the perspective to realize a scalable solid-state quantum computer<sup>30</sup>.

The reason why the *collective* variables of solid state systems usually behave classically is decoherence and the lack of quantum fluctuations which allow the preparation of generically non-classical states. As will be detailed in a later section, the reason for this is coupling to an environment with many degrees of freedom and low-lying excitations. This is *the* main challenge in designing solid-state qubits. A number of proposals has been brought forward, which can be roughly classified in two classes: Spin quantum computing using a controlled exchange interaction such as in Phosphorus in Silicon<sup>31</sup> and spins in quantum dots<sup>32</sup>, and pseudospin quantum computing, where two-state systems other than spin are used such as charge states in quantum dots and superconducting quantum bits. The former promise very long coherence times but are difficult to fabricate and read-out, thus, the experimental realizations are on a rather pioneering stage<sup>33,34</sup>, but the possibilities are enormous<sup>35,36,37</sup>. The status of the latter will be detailed in the following sections of this chapter.

### 3. Superconductivity and the Josephson effect

One specific class of promising qubit implementations is based on superconducting Josephson junctions.

Superconductivity has been discovered already in 1911<sup>38</sup>. It manifests itself by vanishing electrical DC-resistance and by perfect diamagnetism.

The theoretical understanding of superconductivity is now very mature<sup>39,40,41,42</sup>. Already the phenomenological London theory<sup>43</sup> of superconducting electrodynamics describes many superconducting phenomena rather well. Its modern formulation can be derived microscopically and accounts for the fact that superconducting phenomena can be described by the dynamics of a single particle-like wavefunction which describes the collective properties of *all* superconducting electrons. In the presence of an attractive effective interaction, the conduction electrons form Cooper pairs, which condense in momentum space into a collective ground state.

Thus, the “superconducting electrons” of the phenomenological theories are Cooper pairs whose charge is twice the elementary charge. The attractive interactions between electrons in metallic superconductors is phonon-mediated. In superconducting metals, this indirect interaction dominates over the Coulomb repulsion, which is screened and whose phase space is usually restricted by the Pauli principle.

Superconductivity is in itself a macroscopic quantum phenomenon: The simple manifestations of superconductivity such as flux quantization<sup>44</sup> and persistent currents are quantum properties of the condensate wavefunction. This wavefunction is occupied by a macroscopic number of particles. However, in bulk superconductors the wavefunction itself is well-defined and the collective variables, number and phase, do not have quantum uncertainties. The elementary excitations of superconductors are quasiparticles. They are separated from the condensate by an energy gap  $\Delta$ . This can be identified with the order-parameter of Ginzburg-Landau theory<sup>a</sup>.

The gap of the elementary excitations makes superconductors attractive for solid-state quantum computation: The elementary electronic excitations are costly in energy and can be suppressed at low temperatures. At these low temperatures, also the lattice vibrations are frozen out. Thus, conventional superconductors promise to have very low intrinsic decoherence<sup>45</sup> although phonons may play a role<sup>46</sup>.

The Josephson effect<sup>47</sup> is recognized as a hallmark of superconductivity. Its basic statement is that Cooper pairs can coherently tunnel between two superconductors connected by a weak link<sup>48,49</sup>. This gives rise to a supercurrent which is controlled by the difference of the phases of the order parameter in the two superconductors  $\phi = \phi_1 - \phi_2$ . For weak coupling between the superconductors, which will be assumed henceforth unless stated otherwise<sup>50</sup>, the current-phase-relation is sinusoidal,

$$I = I_c \sin \phi. \quad (1)$$

This is the first Josephson equation. From basic consideration of gauge invariance, one can derive the second Josephson relation, which connects the time evolution of the phase difference  $\phi$  with the difference in chemical potential of the Cooper pairs

$$\hbar \dot{\phi} = 2eV. \quad (2)$$

---

<sup>a</sup>In some cases, such as superconductors with magnetic impurities or high-temperature-superconductors close to surfaces, one still keeps an order parameter  $\Delta$ , although excitations below  $\Delta$  exist

The Josephson effect has first been microscopically derived from the BCS theory and the tunneling Hamiltonian by Josephson. Later, a number of pedagogical derivations have appeared, which do *not* contain details of BCS theory and hence outline that the Josephson effect is a universal phenomenon whenever two spatially separated coherent wave functions are connected by a weak link<sup>27,51,52</sup>. In fact, Josephson effects have been observed in systems like superfluid Helium 3 and 4<sup>53,54</sup>, Bose-Einstein-condensates<sup>55</sup>, and molecular junctions<sup>56</sup>.

Real Josephson junctions contain more possibilities to transport charge than the supercurrent. The main mechanisms are:

i) A resistive channel formed by transport of quasiparticles. In tunnel junctions, this contribution is strongly gapped. Thus, at low  $T$  and  $V$ , the effective resistance is very high. In real junctions, there is usually an increased subgap conductance due to barrier defects.

ii) A displacement channel through the effective capacitance of the junction. This capacitance is essentially the parallel plate capacitance between the superconductors. This can be rather big as tunnel junctions are typically fabricated in an overlap geometry as discussed in section 5.1.

Nota bene that one can, by combining the two Josephson equations, interpret the small-signal response of the superconducting channel as a nonlinear inductance: Following eq. (2)  $\phi$  is proportional to the time-integral of a voltage and can hence be interpreted as dimensionless magnetic flux,  $\phi = 2\pi\Phi/\Phi_0$ , where  $\Phi_0 = h/2e \simeq 2 \cdot 10^{-15}\text{Vs}$  is the superconducting flux quantum. Thus, we can linearize eq. (1) as  $I(\Phi + \delta\Phi) = I_c \sin(2\pi\Phi/\Phi_0) + \delta\Phi/L_J$ , or  $\delta I = \delta\Phi/L_J(\Phi)$ . This defines a kinetic inductance,  $L_J(\Phi) = \Phi_0/[2\pi I_c \cos(2\pi\Phi/\Phi_0)]$ <sup>57,58</sup>.

These ingredients can be put together into the famous resistively and capacitively shunted junction (RCSJ) model. It results from Kirchhoff's laws and results in a total current  $I$

$$I_c \sin \phi + \frac{1}{R} \frac{\Phi_0}{2\pi} \dot{\phi} + C \frac{\Phi_0}{2\pi} \ddot{\phi} - I = \delta I(t). \quad (3)$$

where  $\delta I(t)$  is current noise. This constitutes the classical equation of motion of a Josephson junction. The ratio of the coefficients in this model can be described by two parameters: The plasma frequency  $\Omega_{P0} = (L_J(0)C)^{-1/2} = \sqrt{2\pi I_c/C\Phi_0}$  and the McCumber damping parameter  $\beta_c = RC/(L_J/R) = CR^2 I_c/\Phi_0$ . The junction is underdamped if  $\beta_c \gg 1$ . This model has been extensively studied in the classical regime<sup>49,57,58</sup>. It has been derived, in a generalized form, from BCS theory<sup>59</sup>.

Aside from these intrinsic elements, one can of course fabricate an ar-

tifical shunting circuit on-chip in order to influence the dynamics of the junction.

Already on the classical side, Josephson junction circuits enjoy a huge variety of applications. Superconducting quantum interference devices, SQUIDS<sup>60</sup>, are used as ultrasensitive magnetometers and can be used e.g. for measuring brain activity, destruction-free material diagnosis, detection of astrophysical phenomena, high-sensitivity amplifiers, classical flux logic etc. As they are largely controlled by fundamental constants of nature such as  $e$  and  $\hbar$  and, using eq. (2) can convert frequency into current, Josephson devices also have various applications in metrology<sup>61</sup>.

#### 4. Superconducting quantum junctions

In this section, we will derive the macroscopic Hamilton operator of a Josephson junction and the ideas behind it. In the next chapter, we will review several methods to use these junctions in qubits.

Without dissipation as introduced by a shunt conductance (i.e. assuming  $R = \infty$ ), we can rewrite eq. (3) as

$$\frac{\Phi_0}{2\pi} C \ddot{\phi} = I - I_c \sin \phi. \quad (4)$$

This is the equation of motion of a particle with coordinate  $\phi$  and mass  $C(\Phi_0/2\pi)^2$  in a tilted washboard potential  $U(\phi) = -I\phi\frac{\Phi_0}{2\pi} - E_J \cos \phi$  where  $E_J = I_c\Phi_0/2\pi$  is the Josephson energy. We can introduce a Lagrangian

$$L(\phi, \dot{\phi}) = \frac{C}{2} \left( \frac{\Phi_0}{2\pi} \right)^2 \dot{\phi}^2 - U(\phi) \quad (5)$$

whose Euler-Lagrange equation is the correct equation of motion eq. (4). The first term, which plays the role of a kinetic energy, can be interpreted as charging energy,  $E_{\text{ch}}^{(Q)} = \frac{Q^2}{2C}$ , where we have introduced the charge on a capacitor  $Q = \frac{\Phi_0}{2\pi} C \dot{\phi} = CV$ . It follows, that  $\frac{\Phi_0}{2\pi} Q = \frac{\partial L}{\partial \dot{\phi}}$ , i.e. it is proportional to the canonical momentum to  $\phi$ . The Hamilton function equivalent to eq. (5) reads

$$H(\phi, Q) = \frac{Q^2}{2C} + U(\phi). \quad (6)$$

So far, we have been treating  $Q$  and  $\phi$  as classical variables. Following the canonical quantization procedure, we can readily quantize eq. (6) by identifying  $\phi$  and  $Q$  with operators

$$\hat{H} = \frac{\hat{Q}^2}{2C} + U(\hat{\phi}) \quad \frac{\Phi_0}{2\pi} [e^{\pm i\hat{\phi}}, \hat{Q}] = \mp \hbar e^{\pm i\hat{\phi}}. \quad (7)$$

This specific form of the commutator would reduce to the usual canonical commutator if  $\phi$  were not a compact variable<sup>62</sup>. For  $2\pi$ -periodic potentials, this commutator is equivalent to the canonical commutator  $\frac{\Phi_0}{2\pi} [\hat{\phi}, \hat{Q}] = i\hbar$ . This is the basis of the macroscopic quantum theory of Josephson junctions. Eq. (7) specifically predicts that both  $\phi$  and  $Q$  experience quantum fluctuations and cannot be both defined with arbitrary precision; instead, they are limited by a Heisenberg uncertainty relation<sup>40,63</sup>. Typically, the energy scales  $E_J$  and  $E_{\text{ch}} = \frac{2e^2}{C}$  determine the appropriate starting point for describing the junction. For  $E_J \gg E_{\text{ch}}$  the phase fluctuations are weak, the elementary excitations are quantum vortices, and the charge wildly fluctuates. Junctions of this kind are often termed “classical”. In the opposite regime the charge is almost a good quantum number and the phase shows strong fluctuations, these are “quantum” junctions. Using the junction area  $A$ , one can estimate  $E_J \propto I_c \propto A$  whereas  $E_{\text{ch}} \propto 1/C \propto 1/A$ , thus  $E_J/E_{\text{ch}} \propto A^2$  and quantum junctions are typically much smaller in area than classical ones. One can show that the charge and the vortex side are dual and one can observe competing order and quantum phase transitions at  $E_J \simeq E_{\text{ch}}$ <sup>64</sup>.

In order to introduce damping and decoherence in a Lagrangian / Hamiltonian formalism, one has to introduce extra degrees of freedom, typically a bath of harmonic oscillators coupling to the junction variables<sup>65,66</sup>. These unobserved degrees of freedom have to be integrated out when making physical predictions for the junction alone. This has been pioneered for a single Josephson junction by Caldeira and Leggett<sup>67,68</sup>. We will now concentrate on junctions with very low intrinsic damping and will describe the remaining dissipation in a way which is compatible with quantum computing in a later section.

For building a quantum bit one has to make sure that single-qubit rotations are possible. This is ensured when the Hamiltonian has off-diagonal terms in the basis of externally controllable variables. Here this means that one has to make sure that *both* variables fluctuate sufficiently, i.e. if a charge-based device is used, one has to provide enough charge fluctuations and vice versa. Several realizations and proposals which accomplish this have been brought forward so far. These range from large single junctions<sup>69,70,71</sup>, highly inductive loops (RF-SQUIDS)<sup>24,72</sup> and small loops<sup>73,74,75,76</sup>, which are flux-based devices to Cooper pair boxes<sup>30,77,78,79,80</sup>, which are charge-based. Other devices combine charge and phase fluctuations with comparable strength and operate in between<sup>81</sup>. Other proposals use the specific properties of unconventional superconductors<sup>82,83</sup> or large

arrays<sup>84</sup>.

## 5. Different types of superconducting qubits

In this section, we will describe different classes of the Josephson quantum bit along with their experimental status. Superconducting qubits can be divided into roughly three groups: “charge”, “phase”, and “flux” qubits. As mentioned in the previous sections, the common essential element of the superconducting qubit is the mesoscopic scale Josephson junction. In order to prepare a qubit, we need well defined quantum two state system whose intrinsic energy scales are lower than the superconducting energy gap and to a high degree isolated from the outside world. The relevant two energy scale to describe a junction are the Josephson energy  $E_J$  and the charging energy  $E_{ch}$  of the junction for a single Cooper pairs. In the case of junctions made from aluminum thin films, which is the most common technology in the field, these energy scales become comparable typically in the regime of sub-micron sized junctions. So the superconducting Josephson qubit is basically a nonlinear electronic circuit made of superconductor with submicron width and thickness, which we can fabricate by the modern electron beam (EB) lithography and shadow evaporation technique<sup>85</sup>.

### 5.1. Sample preparation

Before mentioning the different qubit design, here, we will briefly mention the most popular process to fabricate the aluminum Josephson junction. First, one has to prepare the double layered resist structure with two different kind of polymers on the thermally oxidized silicon substrate. As illustrated in Fig. 1, the upper thin layer is made of less EB sensitive posi-typed resist. The lower spacer layer is made of more EB sensitive posi-typed resist. After EB pattern writing and developping process with chemical developer, we get a well defined bridge pattern with a nice undercut in the lower layer. Then, the first few tens of nm thick aluminum layer is evaporated from an angle  $-\theta$  from the vertical line. Next, the sample is exposed to dilute oxygen gas. We expect the very thin natural alumina tunnel barrier layer to cover the surface of the fresh aluminum thin film. After purging the oxygen gas, the top aluminum layer is evaporated from the angle of  $\theta$ . Assuming the thickness of the lower spacer layer is  $h$ , the distance between two pieces of evaporated aluminum pattern is  $d = 2h \tan \theta$ . By designing  $h$  and  $\theta$  in advance, we get submicron scale Al/Al<sub>2</sub>O<sub>3</sub>/Al Josephson junction through the lift-off process. This Dolan method<sup>85</sup> has been widely used in

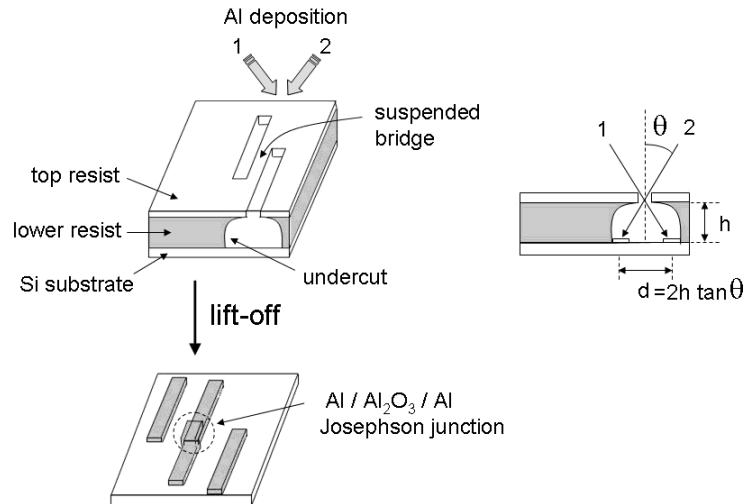


Figure 1. Illustration of suspended bridge and shadow evaporation technique .

reliably making small Josephson junctions over a quarter century.

### 5.2. The flux qubit

A paradigmatic type of Josephson qubit is a flux qubit. It descends from the mesoscopic scale rf-SQUID first introduced by A. J. Leggett to discuss macroscopic quantum tunneling and macroscopic quantum coherence in his groundbreaking paper<sup>23</sup> a quarter century ago.

We will now describe the contemporary version of this device in more detail, namely the persistent current quantum bit, which is phase-based and uses a small loop. This device has been proposed at TU Delft and MIT. As all approaches it has its specific strengths and weaknesses. Most of the theoretical work compiled in the later sections are motivated by this device, but the main ideas can be described in terms of universal Hamiltonians and can be applied to other setups as well.

The flux qubit, fig. 2, consists of a micrometer-sized superconducting loop, which is interrupted by three Josephson tunnel junctions made from the same, conventional technology: Two of equal size, one smaller by a

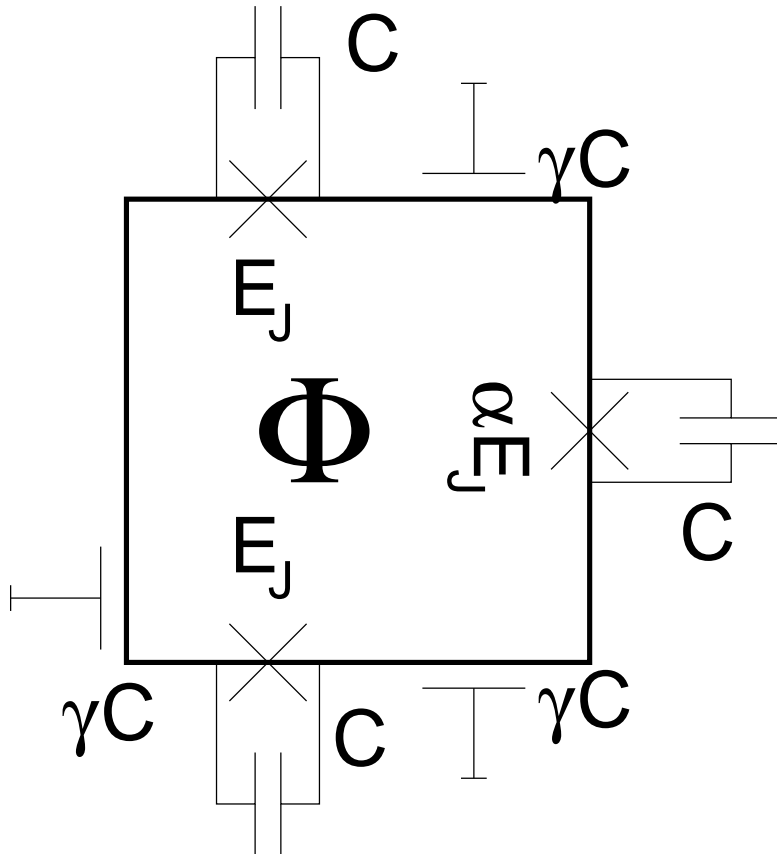


Figure 2. The circuit diagram of a flux qubit threaded by a magnetic flux  $\Phi$ , including three Josephson junctions (crosses) and all geometric and stray capacitances .

factor  $\alpha \simeq 0.8$ . The loop dimensions are chosen such that the geometric self-inductance of the loop does not play any significant role. The loop is penetrated by a magnetic flux of size  $\Phi_x$ , which imposes the quantization condition  $\phi_1 + \phi_2 + \phi_3 = f$ , where  $f = (2\pi\Phi/\Phi_0) \bmod 2\pi$  is the magnetic frustration, for the phases across the three junctions. Thus we can eliminate  $\phi_3$ , the phase across the weaker junction, and obtain the potential energy

$$U = E_J (-\cos \phi_1 - \cos \phi_2 - \alpha \cos(f + \phi_1 - \phi_2)). \quad (8)$$

This potential is plotted in figure 4. The potential is periodic and possesses a hexagonal pattern of minima separated by potential wells. The energy difference of adjacent minima can be tuned through the external flux: They

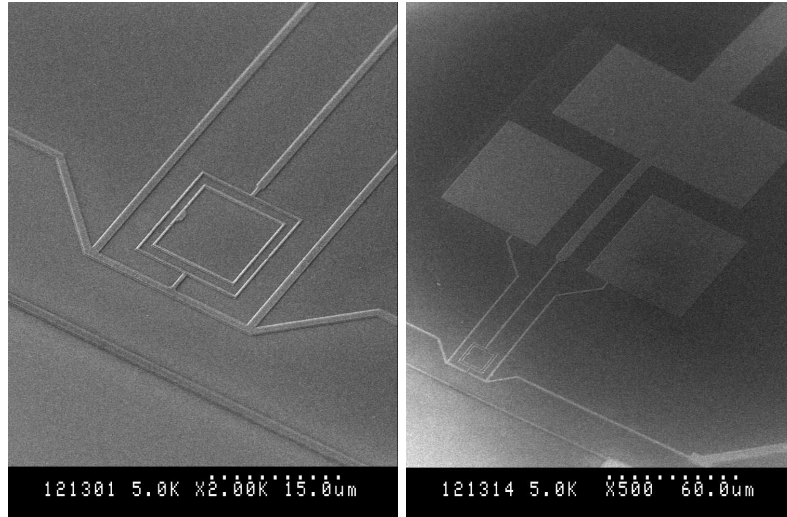


Figure 3. SEM photographs of a flux qubit fabricated at NTT-BRL Atsugi Labs. The aluminium thin film sample (thickness  $\sim 0.1\mu\text{m}$ ) is fabricated on a thermally oxidized silicon substrate with standard electron beam lithography and subsequent shadow evaporation of aluminium. The qubit is the inner square loop enclosed by the quantum detector SQUID which are clearly seen in the left close-up view. In the right photo, the square plates at the top of the picture are the top plates of the on-chip capacitors separated by an aluminium oxide insulator layer from the larger bottom plate. The qubit is controlled through the oscillating magnetic flux produced by an ac-current through the on-chip microwave line which is  $15\mu\text{m}$  away from the qubit.

are degenerate at  $\Phi = \Phi_0/2$ . From choosing one of the Josephson junctions smaller than the others, one direction is introduced in which the potential barrier is substantially smaller than in the other directions. The state in the minima correspond to clockwise and counterclockwise circulating current respectively.

The charging energy can be evaluated from Kirchhoff's laws. The result is written using vectors in the two dimensional  $\{\phi_1, \phi_2\}$  and  $\{Q_1, Q_2\}$  coordinate-space as

$$E_{\text{kin}} = 2e^2 \vec{Q}^T \mathbf{C}_M^{-1} \vec{Q}. \quad (9)$$

with a capacitance matrix

$$\mathbf{C}_M = C \begin{pmatrix} 1 + \alpha + \gamma & -\alpha \\ -\alpha & 1 + \alpha + \gamma \end{pmatrix}. \quad (10)$$

Here,  $\gamma$  is the ratio of the stray capacitances to ground over the junction capacitances, as seen in figure 2.

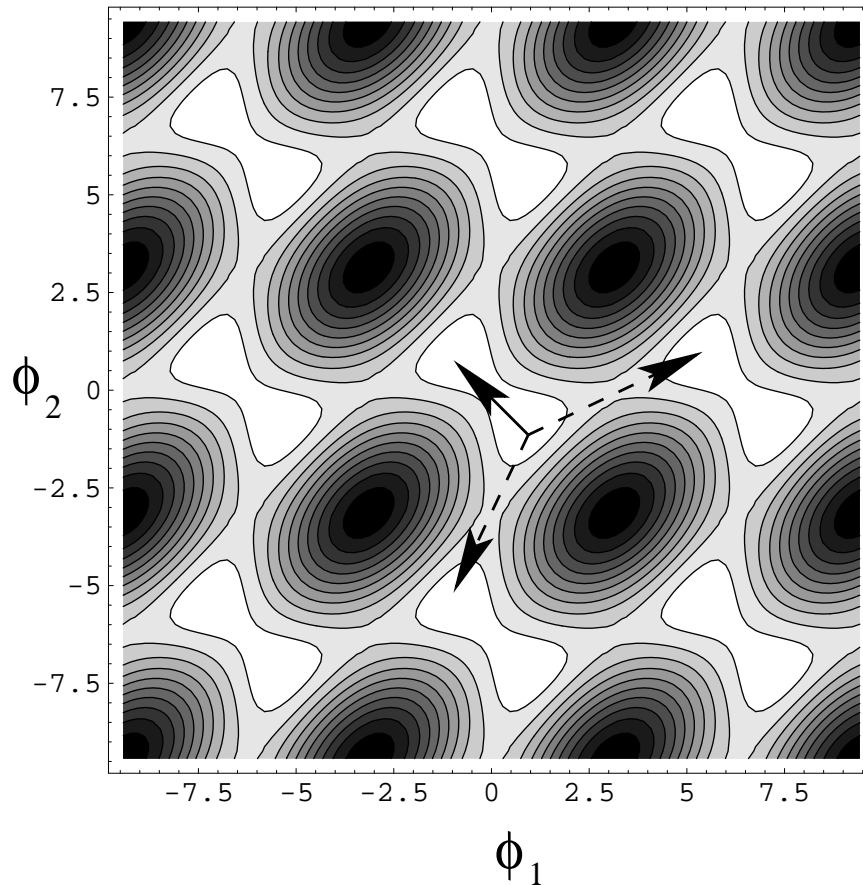


Figure 4. The potential landscape for a flux qubit as a function of the phases across the identical junctions, taking  $\alpha = 0.8$ . The solid arrow indicates an easy tunneling path whereas the dashed lines indicate hard directions.

Carefully choosing appropriate parameters, one can reach a situation with exactly one bound state per minimum, where the tunneling amplitude along the easy direction is substantial and is strongly suppressed along the other directions. At low energies the dynamics of the system can be described in a two-state approximation in the basis of the states localized in the potential minima, the classical states,

$$\hat{H}_2 = \frac{1}{2} \begin{pmatrix} \epsilon & \Delta \\ \Delta & -\epsilon \end{pmatrix}. \quad (11)$$

The energy bias  $\epsilon$  can be steered through the external flux following  $\epsilon \simeq I_q(\Phi - \Phi_0/2)$ , where  $I_q$  is the modulus of the circulating current in the classical states. Thus, the quantum dynamics of the device can be controlled by the external flux.

The tunnel splitting  $\Delta$  can be made tunable by splitting the small junction into two parallel junctions, a DC-SQUID, which acts as an effective single junction whose Josephson coupling  $E_J(\Phi_2) = 2E_{J,0} \cos(\pi\Phi_2/\Phi_0)$  can be tuned by the flux  $\Phi_2$  through this loop between the sum of the two couplings  $2E_{J,0}$  and zero. Such a tunable  $\Delta$  is desirable in a number of, but not in all, quantum computing protocols. The state of the system can be read out by measuring the extra magnetic flux produced by the circulating current through a very sensitive magnetometer: a SQUID<sup>60</sup>. Such a magnetometer works as a tunable junction as just described:  $E_J$  depends on the flux through the loop and can be measured electronically. The SQUID-readout corresponds to a measurement of  $\hat{\sigma}_z$ . Figure 3 shows micrographs of real devices together with their read-out apparatus.

The flux qubit is thus a well-defined quantum system that can perform single-qubit rotations. All other ingredients demanded by DiVincenzo's original five criteria can also be met, which will be detailed more later in this chapter. Note that eq. (11) predicts that superpositions of current states can be prepared close to  $f = \pi/2$ . The current states involve up to  $10^{10}$  electrons. Thus, these are superpositions of large objects. This does not yet imply that these states correspond to huge Schrödinger's cats: For analyzing this question one has to carefully evaluate the distance in Hilbert space between the two states, which is a by far more subtle issue<sup>86,87</sup>.

Note that the analysis here for simplicity neglected self-inductances, which can be included and does not change the overall picture<sup>88,89</sup>

In the advanced flux qubit layout shown in Figure 3 there are two important control parameters of the circuit : the externally applied bias magnetic flux  $\Phi_{\text{ext}}$  and the bias current through the SQUID  $I_b$ . In the flux qubit illustrated in Fig. 5, qubit and SQUID share two edges in order to use the kinetic inductance (the kinetic energy of the Cooper pairs in a line, similar to the kinetic inductance of a junction, see section 3) to increase the coupling strength. This also automatically enables to adiabatically shift the flux bias during the  $I_b$  pulse for qubit state readout just after operating qubit at the *optimal* point. Taking into account that this device is made from a double layer structure and there are odd number junctions in a qubit loop, the persistent currents in the sharing edges do not have to flow in the same layer, whereas the bias currents  $I_b$  through the SQUID flow in the

same lower layer. Unfortunately, this fact causes considerable asymmetric coupling due to kinetic inductance of the qubit and SQUID<sup>90</sup>. Thus the current noise via  $I_b$  through the SQUID can be dominant even at optimum flux bias point where  $\frac{dE_{01}}{d\Phi_{\text{ext}}} = 0$ . In general, this type of asymmetry always exists even in the system of original type flux qubit surrounded by a SQUID as shown in Fig.3 top if there is difference in critical current of two Josephson junctions in the SQUID.

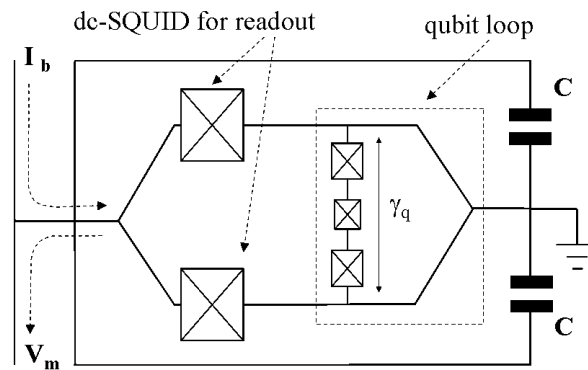


Figure 5. Schematic circuit diagram of the advanced version of the Delft type flux qubit. The qubit loop and the SQUID are now galvanically connected. The SQUID is shunted by additional capacitors  $C$ .  $I_b$  is the bias current and  $V_m$  the detection voltage. .

To overcome these difficulties, the two complementary strategies to protect the qubit from these decoherence sources are employed. One consists in biasing the qubit so that its resonance frequency is stationary with respect to the control parameters (*optimal point*), see section 7.1 ; the second consists in *decoupling* the qubit from current noise by choosing a proper bias current through the SQUID, see section 7.3. Using these strategies, finally at the decoupled optimal point, long spin-echo decay times of up to  $4 \mu\text{s}$  were successfully demonstrated<sup>91</sup>.

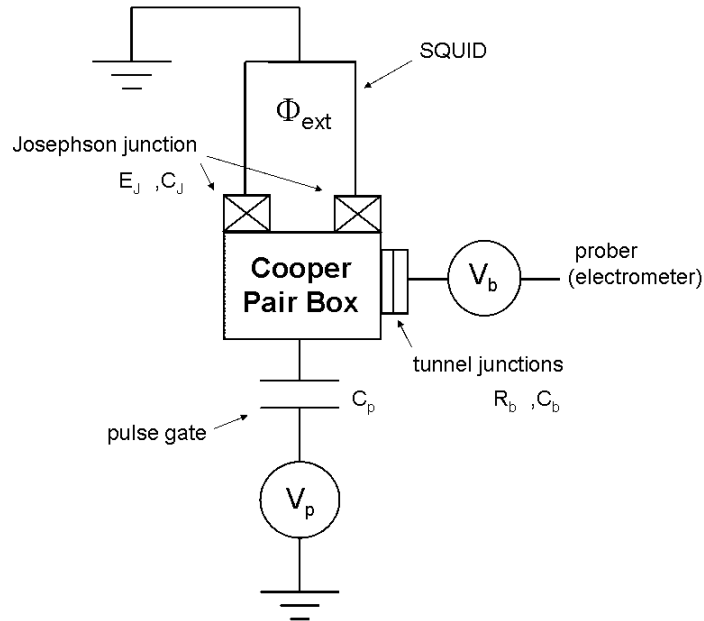


Figure 6. Josephson charge qubit. The central component is a tiny superconducting island called Cooper pair box equipped with small Josephson junction(s) where the charging energy dominates the Josephson energy i.e.,  $E_{ch} > E_J$ . This  $E_J$  value can be tunable by changing the externally applied magnetic flux  $\Phi_{ext}$  in the SQUID loop. The qubit energy is a function of both gate induced charge  $n_g$  and  $\Phi_{ext}$ . The qubit state is controlled by changing  $n_g$  or applying resonant microwave pulse from the onchip RF-line

### 5.3. Other designs

Let's have a look at different schemes of superconducting qubits, one by one. First, as illustrated in Fig. 6, the essential component of the "charge" qubit is a Cooper pair box, a submicron scale superconducting island which is connected to the ground via small Josephson junction. Here, the box is in the charging energy dominant regime  $E_{ch} > E_J$ . In order to tune the  $\frac{E_J}{E_{ch}}$  ratio of the system, this Josephson junction can be separated into two parallel junctions forming a SQUID then one can manipulate  $E_J$  value by controlling the magnetic flux  $\Phi_{ext}$  which penetrates the SQUID loop. In addition to the Josephson junctions, the qubit is also equipped with two lines. One is a probe electrode as a measurement readout line which is weakly tunnel coupled to the Cooper pair box through a thicker oxide layer

shown as a tunnel junction in Fig. 6. The other one is a control pulse gate which is spatially separated from the Cooper pair box and only capacitively coupled to it. In the charge qubit, a good quantum number is a number of excess Cooper pairs  $|n\rangle$  in the box. If one can control the gate voltage precisely enough, then one can change the induced charge  $n_g$  by the gate voltage. The the two states  $|0\rangle$  and  $|1\rangle$  implement a qubit in this system: they would be classically degenerate when  $n_g = 0.5$  but are coupled through  $E_J$  and

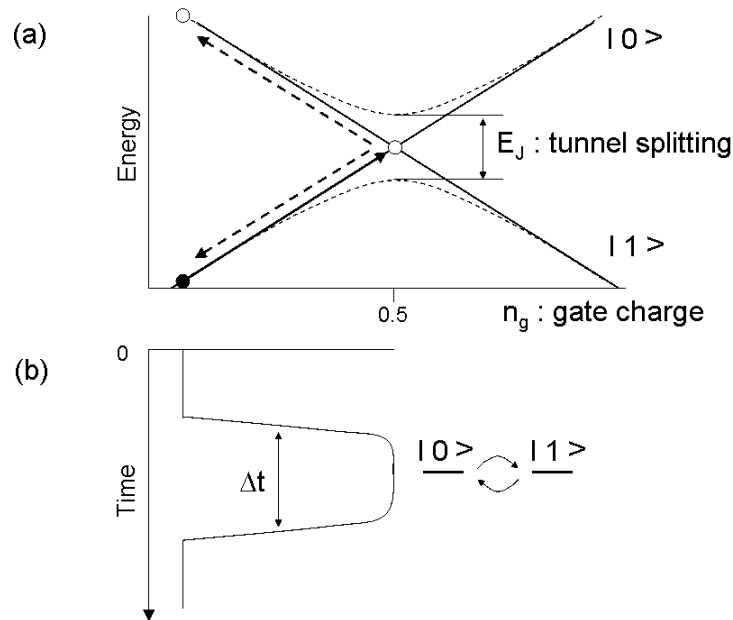


Figure 7. Energy diagram (a) and the control scheme (b) of the Josephson charge qubit. The qubit is controlled via the gate induced charge  $n_g$  in the Cooper pair box by applying a fast (non-adiabatic) voltage pulse from the pulse gate. (a) Initially, qubit state is  $|0\rangle$  (shown as a black dot). Next, bring the qubit state to the degeneracy point ( $n_g = 0.5$ ) by the non-adiabatic gate pulse whose rise and fall time is shorter than the time scale determined by the interaction energy  $\frac{\hbar}{E_J}$ . (b) Qubit state starts quantum oscillation between  $|0\rangle$  and  $|1\rangle$  during the time period of  $\Delta t$ .

However, the Josephson tunneling energy  $E_J$  will lift the degeneracy illustrated in Fig. 7(a). The NEC group prepared charge state  $|0\rangle$  at  $n_g = 0.5$  as shown in Fig. 7(b). Using a non-adiabatic (very fast on the scale of the

qubit level splitting) gate pulse with rise and fall time of 30 ps and  $\Delta t = 80$  ps  $\sim 2$  ns duration, they then succeeded in observing internal coherent oscillation between two energy eigenstates<sup>77</sup> which are shown as the dotted curves in the Fig. 7(a). With an array of pulses with a repetition time longer than the relaxation time, one can repeat the pulse operation many times and measure the direct current through the probe junction which would reflect the population in  $|1\rangle$  after each pulse operation. The experiment demonstrated quantum oscillation with a period of  $\frac{h}{E_J}$  up to 2 ns. This was the first example of the long sought evidence of macroscopic quantum coherence<sup>92</sup>. Other than the gate pulse operation, this type of qubit can be also operated by the resonant microwave pulse<sup>93</sup>.

It is worth mentioning that the echo technique described in section 7.6 works very effectively in the charge qubit. In fact, the coherence time during free evolution  $T_2^*$  was markedly improved more than an order of magnitude<sup>78</sup> i.e., from 0.1 ns to the order of nanoseconds.

This implies the main origin of dephasing in this charge qubit can be ascribed to the low frequency charge noise generated by the random motion of background offset charges, see section 7 of this chapter.

A further type of qubit is the phase qubit which is illustrated in Fig. 8(a). The Josephson phase qubit is a single Josephson junction with an extremely precise current bias. In this layout, the lowest two quantum levels in a washboard potential shown in Fig. 8(b) are used to implement a qubit. The quantum coherent oscillation of the phase qubit were first observed by Martinis<sup>69</sup> and Yu<sup>70</sup> independently. The quantum properties of current biased Josephson junction are well established<sup>94</sup>. As long as the dc voltage across the junction is zero, the nonlinear Josephson inductance and the junction capacitance form an anharmonic LC-resonator. The two lowest quantized energy levels are the states of the qubit. By design the energy separation  $E_{01}$  of these lowest two states can be set much larger than the operating temperature  $E_{01} \sim 10k_B T$ . The sequence of initialization, operation and readout of the qubit is schematically illustrated in Fig. 8(c). In order to keep only a few states in an approximate cubic potential, the current bias  $I_{\text{bias}}$  is pulsed for a time  $\sim 50 \mu\text{s}$ , which is typically driven close to the critical current  $I_c$  of the junction. This is an initialization procedure. Then, a microwave pulse resonant with  $E_{01}$  is applied to induce Rabi oscillations. Immediately after the microwave pulse for Rabi oscillation between ground state  $|0\rangle$  and first excited state  $|1\rangle$ , the readout microwave pulse resonant with  $E_{12}$  is applied to the qubit. If and only if the qubit was

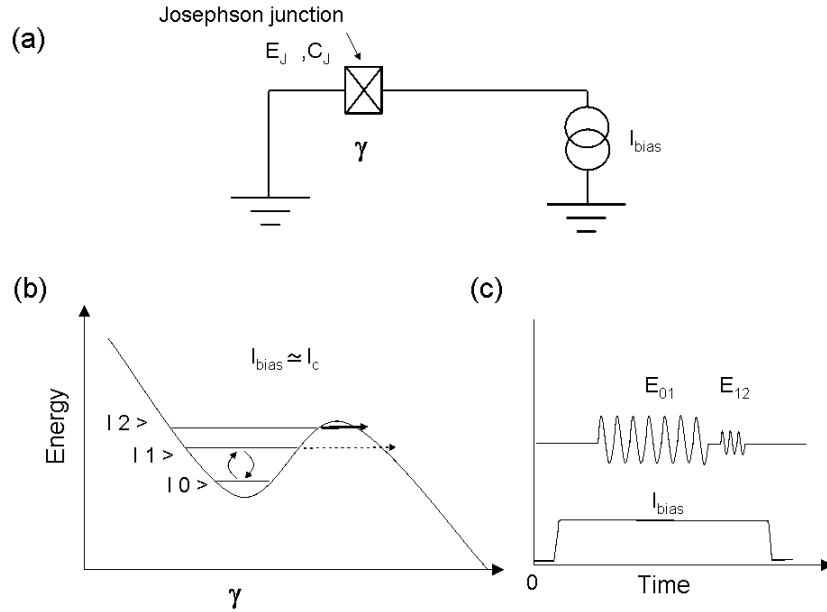


Figure 8. Josephson phase qubit (a) circuit diagram (b) energy diagram (c) timing of the bias current pulse ( $I_{\text{bias}}$ ), microwave pulses for qubit operation (indicated as  $E_{01}$ ) and readout ( $E_{12}$ ).

in state  $|1\rangle$  after the first Rabi pulse, it will proceed to state  $|2\rangle$ . As state  $|2\rangle$  is close to the top of the barrier it easily escapes to the running state and leads to a finite voltage which can be detected. The huge difference in the escape rate between excited levels and the ground state makes it possible to use this as a detector without destabilizing states  $|0\rangle$  and  $|1\rangle$ . Repeating this measurement sequence typically  $10^4 \sim 10^5$  times, one can obtain information about the qubit state through occupation probability of the excited state. As a phase qubit, a rather large ( $\sim 10 \mu\text{m} \times 10 \mu\text{m}$ ) current biased Nb-based Josephson junction has been used. The most significant advantage of the phase qubit is scaling to more complex circuits will be favorable because fabrication and operation of complex superconducting integrated circuit with *large* junctions are well established.

Here, we would like to mention about the quantronium project of the Saclay Quantronics group<sup>81</sup>, a hybrid between the two types described so far. The quantronium circuit is an Al-made Cooper pair box equipped with a SQUID circuit as a readout device. This qubit has two control knobs, the

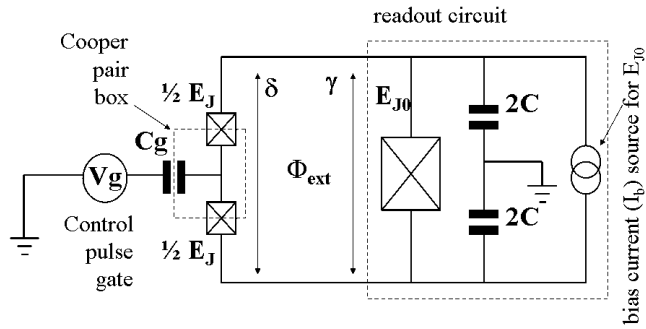


Figure 9. Schematic circuit diagram of the quantronium. A hybrid type design of a charge-qubit (a Cooper-pair box) and a large Josephson junction as a readout circuit which is essentially the same as a phase-qubit. By way of the uniqueness of the phase in a superconducting loop which contains both the Cooper-pair box and the large Josephson junction, the phase difference  $\delta$  across the Cooper pair box, is entangled with the phase difference  $\gamma$  across the large junction which is related with two quantum states of the current biased large Josephson junction. Thus, the state of the charge-qubit is readout through the state of the phase-qubit. This qubit has two control knobs, the gate induced charge  $n_g$  in the Cooper pair box and the bias flux  $\Phi_{\text{ext}}$  of the readout SQUID. The qubit energy is a function of both  $n_g$  and  $\Phi_{\text{ext}}$ . By operating the quantronium at the double extremum condition, they succeeded to obtain remarkably long coherence time during free induction decay  $T_2^* \simeq 0.5\mu\text{s}$ .

gate induced charge  $n_g$  in the Cooper pair box and the bias flux  $\Phi_{\text{ext}}$  of the readout SQUID. The remarkable strategy of this project is to protect qubit from the noise which comes from the electro-magnetic environment by using an *optimal* operating point such as a saddle point or an extremum where  $\frac{\partial E_{01}}{\partial n_g} = 0$  and  $\frac{\partial E_{01}}{\partial \Phi_{\text{ext}}} = 0$ . Moreover, the qubit has a large energy splitting  $\frac{\Delta}{\hbar} \sim 16$  GHz which means rather flat energy dispersion and also intermediate-energy regime i.e.,  $\frac{E_J}{E_{\text{ch}}} \sim 1$  where a circuit is designed to be insensitive to fluctuation of both charge and flux bias. Thanks to the above mentioned ingenuities, they achieved a successful outcome i.e., the Ramsey measurement shows the decay time of  $T_2^* \simeq 0.5\mu\text{s}$  during free evolution by operating the quantronium at the saddle point of the control parameters.

## 6. Experimental achievements

In this section, we are going to overview the status of experimental forefront research of different kind of Josephson qubits.

### 6.1. Single qubit operation

For the single qubit rotations, the resonant microwave driven Rabi oscillations is commonly used<sup>93,69,70,81,75</sup>. On the other hand, the Larmor precession induced by the non-adiabatic fast pulse can be also used<sup>77</sup>. Rabi oscillations with a characteristic decay time of a few microseconds were observed in the phase qubit where current biased large Nb-based Josephson junction ( typically  $\sim 10 \mu\text{m} \times 10 \mu\text{m}$ ) was used<sup>70</sup>.

In quantum computation, it is essential to control each qubit by performing arbitrary unitary operations at will. For one qubit, Rabi oscillation and Ramsey fringes experiments provide information related to the control of the qubit state  $|\Psi\rangle = \cos \frac{\theta}{2} |0\rangle + e^{i\phi} \sin \frac{\theta}{2} |1\rangle$ . In order to achieve noise tolerant qubit operation, NMR-like multi pulse sequence control has been demonstrated in Josephson charge-phase qubit by the Saclay group<sup>?</sup>. However, the observation of the Ramsey fringes of a flux-qubit usually involves a few hundred MHz detuning from the qubit resonant frequency.

The NTT group proposed a new method<sup>95</sup> for observing Ramsey fringes, the phase shift method, which can control the phase of microwave (MW) pulses at the resonant frequency of the qubit. The advantage of this method is that it provides qubit rotation along an arbitrary axis in the  $x$ - $y$  plane and the faster control of the azimuth angle  $\phi$  of a qubit than the conventional detuning method. Figure 10 shows schematic diagrams describing how the qubit vector is operated during the Ramsey fringe experiment with the phase shift technique in a rotating frame.

We assume that the initial state of the qubit is the ground state  $|0\rangle$ . The first resonant  $\frac{\pi}{2}$  pulse ( $\varphi = 0$ ) tips the qubit vector towards the equator with the  $x$ -axis as the rotating axis ( $\hat{H}_{\text{rot}} \propto \hat{\sigma}_x$ ). The qubit vector remains there because we introduce no detuning ( $\omega = \omega_0$ ). After a time  $t_{12}$ , the second resonant  $\frac{\pi}{2}$  pulse with a given phase shift  $\varphi \neq 0$  tips the qubit vector on another axis at an angle  $\varphi$  from the  $x$ -axis. The resulting qubit vector does not reach the south pole ( $|1\rangle$ ) of the Bloch sphere. The detector SQUID switches by picking up the  $z$ -component of the final qubit vector after the trigger readout pulse. Repeating this sequence typically 10,000 times, with a fixed  $t_{12}$ , we obtain the switching probability. Figure 11 shows the damped sinusoidal oscillation obtained by changing the pulse interval

Figure 10. Schematic diagram of qubit vector motion induced by the phase-shifted double  $\frac{\pi}{2}$  on-resonance pulses ( $\omega = \omega_0$ ). It is described in the rotating frame of the qubit Larmor frequency  $\omega_0$ . (a) The qubit vector in the initial state. The qubit is in the ground state  $|0\rangle$ . (b) The first resonant  $\frac{\pi}{2}$  pulse ( $\varphi = 0$ ) tips the qubit vector to the equator. The qubit vector remains there, because the on-resonance pulse is used. (c) The second resonant  $\frac{\pi}{2}$  pulse, in which the phase-shift  $\varphi \neq 0$  is introduced, tips the qubit vector on another axis, which is at an angle  $\varphi$  from the  $x$ -axis. .

$t_{12}$ . The phase shift of the second pulse was programmed from the following relation ;  $\varphi = \omega_0 t_{12} \bmod 2\pi$ . This equation gives a  $2\pi$  phase change to the resonant microwave pulse during a period of  $T = \frac{2\pi}{\omega_0}$ . This means that we introduce a phase shift with the Larmor frequency.

When Ramsey fringes are observed in the conventional way, a few hundred MHz detuning is typically introduced near the qubit Larmor frequency, i.e.,  $\sim 100$  MHz detuning at a Larmor frequency of  $\sim 5$  GHz. With this detuning method, after the first detuned  $\frac{\pi}{2}$  pulse, the qubit vector rotates along the equator of the Bloch sphere with this detuning frequency,  $\sim 100$  MHz<sup>75</sup>. If we use this method to control the qubit azimuth angle, a time of  $\sim 10$  ns is required for every  $2\pi$  azimuth angle rotation of the qubit vector.

Figure 11. On-resonance Ramsey fringes observed by using the phase-shifted double  $\frac{\pi}{2}$  pulse technique. The Larmor frequency is  $\omega/2\pi=11.4$  GHz. The width of the  $\frac{\pi}{2}$  pulse, 5 ns, is determined by Rabi oscillation. An exponentially damped sinusoidal curve fitted with the decay time constant  $T_2 = 0.84$  ns is also shown. .

This operating time cannot be as short as 1 ns, because a detuning of 1 GHz does not work properly. However, with the phase shift technique with the resonant frequency, as we have shown, it is possible to revolve the rotational axis of the qubit vector within the  $xy$ -plane with the frequency above 11 GHz. By way of the well known decomposition of a rotation in three rotations around two orthogonal axes<sup>4</sup>, one can perform quick qubit rotations without using relatively slow free evolution by introducing detuning. In particular, using the relation  $Z(\phi) = X(\frac{\pi}{2})Y(\phi)X(-\frac{\pi}{2})$ , the azimuth angle  $\phi$  rotation on the  $z$ -axis can be decomposed into three successive rotational operations such that  $-\frac{\pi}{2}$  rotation on the  $x$ -axis,  $\phi$  rotation on the  $y$ -axis, and  $\frac{\pi}{2}$  rotation on the  $x$ -axis. If the qubit is driven strongly enough, each  $\frac{\pi}{2}$ -pulse width can be as short as 0.1 ns, therefore the total composite operation  $X(\frac{\pi}{2})Y(\phi)X(-\frac{\pi}{2})$  can be completed in  $\sim 1$  ns. Compared with the conventional detuning method, the phase shift technique provides us with

the opportunity to increase the speed of the qubit unitary gate operation by more than an order of magnitude. This method will save operating time and we can make best use of the precious coherence time.

## 6.2. Coherence time

Remarkable progress has been achieved in strategies to obtain improved coherence time during the free evolution  $T_2^*$ . Two major strategies to protect the qubit from possible decoherence sources are found. One is biasing the qubit so that its resonance frequency is stationary with respect to the control parameters (*optimal point*) which is demonstrated by Saclay group in the “quantronium” project. A sharp line width as narrow as 0.8 MHz was observed in the spectroscopy at the optimal point with the qubit resonant frequency  $\sim 16$ GHz, where a  $Q$ -value over  $2 \times 10^4$  was obtained. Just like the pulsed NMR technique, they obtained an optimised  $T_2^* \simeq 0.5 \mu s$  of their charge-phase qubit from a Ramsey fringe experiment<sup>81</sup>. Now, this strategy is already a common standard in most experimental efforts. The second strategy was applied in the flux-qubit experiment, which consists in *decoupling* the qubit from current noise by choosing a proper bias current through the readout SQUID. Using 4- instead of 3-junction qubit, at the decoupled optimal point, the long spin-echo decay times of  $4 \mu s$  was demonstrated<sup>91</sup>. As these strategies decouple from different sources of  $T_2$  limitation, they conceivably need to be combined to achieve further progress.

In usual experiment, we observe  $T_2$ , the transversal relaxation or dephasing time, is (much) shorter than the energy relaxation time  $T_1$ . From a general consideration, the energy relaxation time  $T_1$  is governed by the noise spectral density  $S(\omega)$  at a frequency corresponding to the qubit level splitting, as described by (12) in chapter 7.1. On the other hand, the phase relaxation time  $T_2$  is governed by the noise spectral density at low frequency limit  $S(0)$  but also contains  $T_1$  (13). In the idealistic situation where  $S(0) \rightarrow 0$ , the relation  $T_2 = 2T_1$  is expected. Recently, JST-RIKEN-NEC group<sup>7</sup> and NTT group<sup>7</sup> have observed the  $T_2 \approx 2T_1$  relation at the optimal operating point.

In the phase qubit, large-gap superconductors such as Nb or NbN have an advantage in suppressing unwanted quasi-particle generation due to thermal activation or due to parasitic circuit resonances inherently excited in the on-chip circuit. However, a lot of anticrossings in the microwave spectra<sup>96</sup> and the observation of real-time oscillations between qubit and resonator<sup>97</sup> reported by the NIST group provide evidence that some kind

of unexpected fluctuators are coupled coherently to the phase qubit. They observed that a number of small such spurious resonators have a distribution in splitting size, with largest one giving a splitting of  $\sim 25$  MHz and an approximate density of 1 major spurious resonance per  $\sim 60$  MHz. When thermally cycled from  $\sim 20$  mK to room temperature, the magnitude and frequency of the spurious resonances changed considerably, whereas cycling to 4 K produces no apparent effect. Furthermore, over 10 qubit devices with the same experimental setup, they found that each qubit has its own unique “fingerprint” of resonance frequencies and splitting strength. From these observations, they ascribed that these spurious resonances are microscopic in origin such as two-level fluctuators within the amorphous oxide tunnel barrier in the Josephson junction which couple to the qubit state through the critical current. This should be one of the origin of similar magnitude of  $1/f$  noise observed over the tunnel junction made from oxide of Al, Nb, PbIn. In that work, it is insisted that improvements in the coherence of all Josephson qubits will require materials research directed at reducing or removing these resonance states that have remained hidden for over 40 years in the conventional junction fabrication technique such as shadow evaporation. Following this warning, the NIST and also the Delft group already started projects to fabricate Josephson junction with greater microscopic uniformity by employing molecular beam epitaxy.

### 6.3. *Different materials*

Here, we mention about two more topics from the material related side of qubit research. Recently, two groups independently succeeded in observation of macroscopic quantum tunneling (MQT) in Josephson junction made of d-wave high- $T_c$  cuprate superconductors. The Chalmers group used YBCO grain boundary biepitaxial junction<sup>98</sup>. The Tohoku university group, using an intrinsic Josephson junction in BSCCO, observed a quantum-classical crossover temperature for MQT of  $T_{MQT} \sim 1$  K<sup>99</sup> which is significantly larger compared with  $T_{MQT} \leq 300$  mK of conventional superconducting material such as Al or Nb. This result indicate the merit of using a superconductor with a larger gap energy scale exceeds the demerit that there are gapless excitations in some directions on the Fermi surface. The other topic is that all  $MgB_2$  tunnel junctions showed Josephson current-voltage characteristics above 20 K<sup>100,7</sup>. The binary compound  $MgB_2$  has  $T_c \sim 40$  K would be another candidate to fabricate noise tolerant qubit which requires a large energy splitting within the superconducting

gap.

#### 6.4. Readout

A good readout visibility is another indispensable condition for quantum computation. The NTT group reported an interesting possibility<sup>101</sup>. They used a detection SQUID with very small Josephson junctions ( $0.1 \mu\text{m} \times 0.1 \mu\text{m}$ ). The qubit signals were measured in a regime of small switching current  $I_{sw}$  of the SQUID, typically less than 100 nA, where the switching current distribution turns out to be particularly narrow. The obtained single-shot data indicate that the qubit state is readout as energy eigenstates rather than current eigenstates although  $I_{sw}$  of the SQUID were used as a detection observable. In this case,  $I_{bias}$  of the SQUID were swept very slowly. The electro-magnetic environment of SQUID was likely to be substantially overdamped. They interpreted their result as follows<sup>102</sup>: the qubit-SQUID interaction energy was so small that the qubit energy eigenstate was readout without being projected onto the current states. In other words, while qubit state is bimodal, however, the SQUID switching current  $I_{sw}$  can take a continuous value. If the qubit energy splitting is larger compared with the qubit-SQUID interaction energy, the SQUID only switches under the influence of magnetic flux created by the qubit.

The RIKEN-NEC group reported that they succeeded in single shot state readout of the Josephson charge qubit by using an onchip superconducting single electron transistor (S-SET)<sup>103</sup>. The quantum bits were transformed into and stored as classical bits (charge quanta) in a dynamic memory cell - a superconducting island. The transformation of state  $|1\rangle$  (differing from state  $|0\rangle$  by an extra Cooper pair) was a result of a controllable quasiparticle tunneling to the island. The charge was then detected by a conventional single-electron transistor, electrostatically decoupled from the qubit. They also studied relaxation dynamics in the system and obtained the readout efficiency of 87 and 93% for  $|1\rangle$  and  $|0\rangle$  states, respectively.

Recently, it has become clear that in the SQUID switching detection type measurement, we lose substantial qubit visibility during relatively slow ramp up process of the SQUID bias current. In fact, by changing the conventional bias readout pulse of 10 ns rise time to faster microwave pulse of 0.5 ns rise time by the resonant activation method, 40% visibility of the flux-qubit was improved up to 65%<sup>104</sup>.

On the other hand, another approaches of qubit state measurement

without switching the SQUID detector are in progress in Yale<sup>105,7</sup> and also in Delft<sup>106</sup>. On the superconducting branch, the SQUID acts as if it is an inductance (Josephson inductance), see section 3. They use the SQUID as an anharmonic LC-resonator and detect resonant frequency shift as a function of applied magnetic flux. The intrinsic flux detection efficiency and backaction are suitable for a fast and nondestructive determination of the quantum state of the qubit. This method will provide an opportunity of quantum non-demolition measurement of a qubit as needed for readout of multiple qubits in a quantum computer.

### 6.5. *Two qubit operation*

After the initial breakthrough in the coherent manipulation of a single Josephson qubit<sup>77</sup>, the next target has been to control entanglement in two-qubit system. The NEC-RIKEN group has reported a controlled-NOT operation in the capacitively coupled two Josephson charge qubits<sup>107</sup>. They could apply fast (rise/fall time 40 ps) voltage pulse to change each qubit state independently. For the input states of  $|10\rangle$  and  $|11\rangle$ , their gate operation was almost ideal. On the other hand, for the input states of  $|00\rangle$  and  $|01\rangle$ , the output states have an unwanted component of  $|00\rangle$  or  $|01\rangle$  with a rather high probability ( $\sim 37\%$ ). According to them, this might be due to the finite rise/fall time (40 ps) of the operation pulse, which increased the unwanted oscillation.

Recently, the NIST-UCSB group has succeeded in simultaneous state measurement of capacitively coupled Josephson phase qubits<sup>108</sup>. They have used simultaneous single-shot measurement of coupled Josephson phase qubits to directly probe interaction of the qubits in the time domain. The concept of measurement crosstalk is introduced, and they showed that its effects are minimized by careful adjustment of the timing of the measurements. They observed an antiphase oscillation of the two-qubit  $|01\rangle$  and  $|10\rangle$  states.

### 6.6. *Cavity QED on a chip*

The alternative way to implement multi qubit gate is using a quantum bus in order to couple arbitrary pair of qubits on demand. This Cirac-Zoller type scheme<sup>13</sup> is used in ion trap systems. Recently, observation of strong coupling in all- solid state implementations of the cavity QED concept using circuit elements were reported by the Delft-NTT-NEC group and the Yale group independently. Delft-NTT-NEC group<sup>109</sup> has observed a flux

qubit strongly coupled to non-linear SQUID oscillator. On the other hand, the Yale group<sup>110</sup> has observed a charge-phase qubit strongly coupled to a dispersive transmission line resonator, which acts as a linear oscillator.

The Yale group also succeeded in observing the ac Stark shift<sup>7</sup> of the qubit level in a single photon resolution. This means, a single photon on average and does not refer to a single photon Fock state. They have demonstrated that the strong coupling of a Cooper pair box to a non-resonant microwave field in an on-chip cavity gives rise to a large qubit dependent shift in the excitation energy of the resonator. As the counteraction, the ac Stark effect also shifts the qubit level separation by about one linewidth per photon at 2% detuning, and the backaction of the fluctuations in the field gives rise to a large broadening of the qubit line.

Very recently, the NTT group has successfully observed time domain vacuum Rabi oscillation in a macroscopic superconducting flux qubit and on-chip linear lumped element LC oscillator system<sup>7</sup>. SEM photograph of the sample is shown in Fig.12(a). The flux-qubit (Fig.12(b)) and the LC-oscillator is inductively coupled. Estimated coupling strength 0.2 GHz is well in the strong coupling regime. The resonance frequency of the LC-oscillator was observed as 4.3 GHz ( $\sim 200$  mK). Experiment was done with temperature of 20 mK, which was well below the smallest excitation energy including the LC-oscillator quantum. As shown in Fig.13,  $\pi$ , and  $2\pi$ -pulse used in the experiment were determined from the Rabi oscillation. Figure14 shows example of the conditional spectroscopy, when qubit energy was biased at 14 GHz. The red- and blue-sideband transition and also driven Rabi oscillations were clearly observed just like trapped ions interacting with their collective normal mode oscillation<sup>7</sup>. We have observed vacuum Rabi oscillations in time domain as follows. Preparing the  $|e, 0\rangle$  state by applying a  $\pi$ -pulse to the ground state  $|g, 0\rangle$  (we adopt the notation |qubit, Fock state of the LC-oscillator)). Immediately after the  $\pi$ -pulse, applied dc-flux bias shift pulse brings the qubit to the resonant point where  $|e, 0\rangle$  and  $|g, 1\rangle$  have the same energy. Here, the rise/fall time of the dc-shift pulse should be adiabatic to the qubit i.e., longer than 0.1 ns, but non-adiabatic to the coupling between qubit and the LC-oscillator i.e., shorter than 5 ns. Then switching probability of the detecting SQUID, which is directly related to the excited state occupation of the qubit, as a function of the time period of resonance condition, we observe a decaying sinusoidal oscillation with frequency  $\Omega_R$  between  $|e, 0\rangle$  and  $|g, 1\rangle$ . By exciting the LC-oscillator very weakly during vacuum Rabi measurement pulse sequence, we confirmed gradual frequency crossover of the Rabi os-

Figure 12. Scanning Electron Micrograph of the sample measured at NTT-BRL Atsugi Labs. (a) SEM picture of a flux qubit together with near-by on-chip elements. Note that the size of the LC-circuit made of shunt capacitor and lead inductance is an order of 0.1 mm large. (b) Close-up view of the central part of the device. A flux qubit with a dc-SQUID; a quantum detector of the qubit state. .

cillation from  $\Omega_R$  to expected higher frequency component  $\sqrt{2}\Omega_R$  which is coming from the coherent oscillation between  $|e, 1\rangle$  and  $|g, 2\rangle$ . This is the first direct evidence of the level quantization of macroscopic LC-resonator. By replacing a Rydberg atom to a flux-qubit and a high-Q cavity to an on-chip LC-oscillator, we will be able to perform cavity QED experiment on a chip where we can enjoy orders of magnitude stronger coupling compared to atomic quantum optics.

Figure 13. Rabi oscillations of the flux-qubit during resonant ( $E = 14$  GHz) microwave pulse, at temperature of 20 mK. The  $\pi$  and  $2\pi$ -pulse for qubit control are determined from Rabi oscillations. The left figure is the close-up of the initial part of the Rabi oscillations framed by the broken line. The amplitude of the Rabi oscillation is  $\sim 25\%$ .

## 7. Decoherence

Coherence is the ability to interfere and is usually associated with the phase of a wave. In optics, light is called incoherent if its propagation can be described by geometrical optics alone<sup>111</sup>. The applicability of such a description clearly depends on the phenomenon being studied and on the scale of observation. The focusing of coherent laser light on large scales can, e.g., still be described by geometrical optics, the interference phenomena of the same laser beam in an interferometer require the use of a wave descrip-

Figure 14. Conditional spectroscopy observed in the qubit-LC oscillator coupled system. The qubit resonant frequency is fixed at  $E = 14$  GHz. The lower (upper) trace is taken when the qubit is in the ground (excited) state. Only the blue- (red-) sideband is observed except for the qubit transition which can be understood by the level scheme of the coupled system. .

tion. In quantum mechanics, the phase under consideration is usually the phase of the wave function and the incoherent limit of the theory is classical physics. Decoherence is the loss of coherence — in quantum mechanics it describes the transition from generically quantum to classical behavior. When describing decoherence, one thus has to clearly specify which quantum interference phenomenon (and which classical counterpart) is being studied. E.g. in a two-state-system (TSS) one can specify the “decoherence of free quantum oscillations” instead of just “decoherence”. We will see that

there are regimes when specific quantum phenomena, such as the formation of superpositions of classical states, are still observable, whereas others, such as real-time interference fringes, are already completely suppressed. In fact, this property of decoherence is important for the coexistence of classical and quantum description of matter e.g. in the large-scale classical description of molecules bound together by the quantum phenomenon of chemical bonding. The understanding of decoherence has huge impact on the general understanding of quantum mechanics<sup>112,113,114</sup>.

Decoherence is an irreversible phenomenon including dissipation of energy and/or the generation of entropy. Consequently decoherence is not a generic part of elementary quantum mechanics based on the Schrödinger equation or its relativistic generalizations, which are all reversible at least in the sense of the CPT-theorem. This apparent contradiction is easily solved in large systems with a thermodynamic number of degrees of freedom: Such a system has a high number of levels and from a general initial state its wave function will follow a complex beating of oscillations whose frequencies are set by all possible transition frequencies  $\omega_{nm} = (E_n - E_m)/\hbar$  between all combinations of levels  $n, m$ . It will return to its initial state after a time  $T$  which satisfies  $T = 2p_{nm}\pi/\omega_{nm}$  for all  $n, m$  with a set of integers  $p_{nm}$ . This time is called Poincaré time and has very large values in thermodynamic systems with (quasi)continuous spectra. Thus, the reversibility cannot be observed in any reasonable experiment. On the other hand, there are always pairs of  $\omega_{nm}$  and  $\omega_{m'n'}$  very close together, such that coherent phenomena between states  $n$  and  $m$  are completely masked by those of states  $m', n'$  and can also not be observed on short time scales. Moreover, observing a system exactly with this precision in a well-defined way requires the repeated preparation of the same microscopic initial state, which is not possible for such a high number of degrees of freedom. In other words: Even though microscopic physics may be reversible and coherent, we are very often not able to observe it.

From the above discussion we can readily understand how coherence and reversibility vanish for large systems. Here, we are however mostly interested in small arrays of qubits, systems with very few (effective) degrees of freedom, and want to understand how they lose their coherence. The type of model invoked is closely related to the above example: The system is extended by coupling the quantum system to an environment (bath) containing a number of macroscopic degrees of freedom, whose detailed initial state is unknown except for its thermodynamical variables. Then one solves the dynamics of the full setup containing the quantum system and the bath. The

solution will depend on the initial state of the bath and by tracing out the average over the ensemble of initial states of the bath, the effective reduced dynamics of the system under the influence of the bath is found. Baths of this kind always occur in nature: Generally, one has to be aware of the fact that the experimental machinery and the control and manipulation instruments can serve as a bath; in fact, even the electromagnetic vacuum is a bath to which energy can be emitted<sup>115</sup>. It is in particular straightforward to identify physical baths in solids: All the “unused” degrees of freedom, typically the lattice and electronic excitations, act as sources of decoherence for the qubit degrees of freedom. Recalling the preceding discussion of superconducting qubits, we note that the ubiquitous natural baths in a solid-state environment are suppressed: lattice vibrations are frozen out and the electronic excitations are gapped: Thus, superconductors are good candidates for maintaining coherence in solid-state qubits.

Due to the necessity to introduce an environment, quantum systems suffering from decoherence are often called “open quantum systems”.

The transition to classical physics manifests itself in at least three ways, which are related but not equivalent. These cases will now be illustrated invoking a system described by a two-state Hamiltonian of the form eq. (11).

Firstly, a system can be by all means coherent and sufficiently isolated from the environment, but the coherent phenomenon manifests itself on an unobservable scale. E.g., we would not be able to observe coherence fringes in the propagation of a ping-pong ball, because the de Broglie wave length of the ball at any reasonable velocity is too small to be observed (at  $v = 1\text{m/s}$  it is on the order of  $10^{-30}\text{m}$ ). In eq. (11), this would occur if the off-diagonal matrix element is so small that one cannot keep  $\epsilon = 0$  with sufficient precision and hence cannot prepare superpositions, or if  $\epsilon \gg \Delta$  such that coherent oscillations are too fast to be observed and/or too small in amplitude. This can be attributed to the fact that the quantum fluctuations leading to the coherent coupling of the classical states (here, the eigenstates of  $\hat{\sigma}_z$ ) are too small. For tunneling systems such as the flux qubit,  $\Delta$  is proportional to the overlap of the basis states in some double-well potential<sup>74</sup>. We can thus associate a small  $\Delta$  with the fact that the basis states are too strongly separated for coherent tunneling. They are hence too distinct - very similar to the fact that the wave functions “alive” and “dead” of Schrödinger’s cat<sup>116</sup> do not overlap. This type of vanishing quantum effects is usually not referred to as decoherence but as macroscopic distinction<sup>87</sup> and has also been termed “false decoherence”<sup>86</sup>.

Secondly, if the system has an appropriate effective Hamiltonian with a sufficiently large off-diagonal matrix element it would be able to show all kinds of quantum coherent interference phenomena leading to fringes or temporal oscillations, such as the coherent oscillations of a two-state system which is initially *not* prepared in an eigenstate of the Hamiltonian eq. (11). Due to the influence of the environment these oscillations lose their phase and are suppressed. This can be understood in an ensemble-average: The system plus the bath propagate together and display a complex beating pattern. As the bath is prepared in somewhat different states in each member of the ensemble, this propagation looks differently for each realization and the quantum subsystem, from a unique initial state, accumulates more and more differences between one realization and the other, until ensemble-averaged quantum properties die out. This ensemble can well be taken in time, by repeating experiments with identical initial states of the quantum subsystem. This phenomenon is called “dephasing”. It does not necessarily involve the exchange of energy with the environment. On the other hand, at long times we expect the system to go into a thermal state described by a diagonal Boltzmann-type density matrix. This process involves energy exchange with the environment and is called relaxation. It takes place if there are no special selection rules and *does* necessarily also lead to dephasing. The thermal state can still involve superpositions of the basis states, if the Hamiltonian has off-diagonal terms. All in all this type of dynamics is called (“generic”) decoherence.

Thirdly even if the system Hamiltonian eq. (11) has substantial off-diagonal elements, coherent tunneling between the classical states can be blocked on all time scales by interaction with the environment. In fact, the system gets dressed by fast degrees of freedom in the environment, i.e. the system states  $|\psi_n\rangle$  have to be replaced by combined states  $|\psi_n\rangle_{\text{eff}} = |\psi_n\rangle \otimes |ENV_n\rangle$ , where  $|ENV_n\rangle$  are the lowest-energy states of the bath under the condition that the quantum system is in state  $|\psi_n\rangle$ . This type of dressing leads to a renormalization of the system Hamiltonian. E.g., in eq. (11),  $\Delta$  gets renormalized to  $\Delta_{\text{eff}}$  when one couples a bath of oscillators to  $\hat{\sigma}_z$ <sup>92,117</sup>. Such renormalization effects are known throughout physics as Lamb shift, Franck-Condon effect etc. , all of which describe the introduction of an effective Hamiltonian whose matrix elements are different from the original ones due to the interaction with some environment. If the bath is infinite and has sufficient spectral weight at all frequencies, the system can undergo a dissipative phase transition<sup>92</sup> which leads to  $\Delta_{\text{eff}} = 0$ , making the system completely classical and localized, similar to

Anderson's orthogonality catastrophe<sup>118</sup> in Fermionic systems. In fact, the dynamics described in the previous paragraph is always governed by  $H_{\text{eff}}$ . In particular, there are no superpositions of classical states left in a thermal mixture. Another way to interpret this is, that the system builds up entanglement with the environment, i.e. any superposition of different  $|\psi_n\rangle_{\text{eff}}, |\psi_m\rangle_{\text{eff}}$  is entangled. If the entanglement is complete, such that the  $|ENV_n\rangle$  are mutually orthogonal, the system cannot tunnel any more between the classical states  ${}_{\text{eff}}\langle\psi_n|\psi_{m\neq n}\rangle_{\text{eff}} \rightarrow 0$ . This is analogous to the first scenario: There the system states themselves are macroscopically distinct, here only the entangled system plus environment states are.

### 7.1. Methods

The discussion in the previous section already indicates the importance of studying noise for understanding decoherence<sup>119,120</sup>. In fact, parts of our results on decoherence can be understood from noise theory alone without a detour via an environmental Hamiltonian. This can be illustrated by the two-state system described by (11), where  $\epsilon$  is noisy,  $\epsilon = \epsilon_0 + \delta\epsilon(t)$ . We can readily solve the associated Schrödinger equation. Even more intuitively we can describe the state of the system by the expectation values of the three components of the spin, and the Schrödinger equation becomes the classical equation of motion of magnetic moment in a fluctuating magnetic field. For each realization of the noise, the system behaves coherently, but the coherent evolution has a noisy component. Averaging over the noise then leads to incoherent evolution. Specifically, two key results can be derived on that level, assuming that  $\delta\epsilon$  can be treated perturbatively<sup>121,122</sup>: The relaxation rate is proportional to the noise spectral density  $S = \langle\{\delta\epsilon(t), \delta\epsilon(0)\}\rangle_{\omega}/2$  at a frequency corresponding to the level splitting  $E = \sqrt{\epsilon^2 + \Delta^2}$

$$\Gamma_r = \frac{1}{T_1} = \frac{\Delta^2}{E^2} S(E). \quad (12)$$

Flip-less decoherence contains a zero energy exchange (zero frequency) contribution as well<sup>123,124,30</sup>

$$\Gamma_{\phi} = \frac{1}{T_2} = \Gamma_r/2 + \frac{\epsilon^2}{E^2} S(0). \quad (13)$$

These results can be intuitively interpreted: The system can relax by dissipating all its energy  $E$  into an environmental Boson. Due to the weakness of the coupling, multi-Boson processes are strongly suppressed. The relaxation also dephases the state. Moreover, dephasing can occur due to the

coupling to low-frequency modes which do not change the energy of the system. These expressions for relaxation and dephasing have also been found by studying the Hamiltonian of our qubit coupled to a damped oscillator, using a Markovian master equation approach by Tian *et al.*<sup>125</sup> (based on work by Garg *et al.*<sup>126</sup>).

The expressions (12) and (13) have prefactors  $(\frac{\Delta}{E})^2$  and  $(\frac{\epsilon}{E})^2$  that depend on the tunnel splitting  $\Delta$  and the energy bias  $\epsilon$ . These factors correspond to the angles between noise and eigen states usually introduced in NMR<sup>127</sup> and account for the effect that the qubit's magnetic dipole radiation is strongest where the flux in the qubit  $\Phi_q = \frac{1}{2}\Phi_0$  (i. e.  $(\frac{\Delta}{E})$  maximal), and that the level separation  $\nu$  is insensitive to flux noise at this point (i. e.  $\frac{\partial\nu}{\partial\epsilon} = (\frac{\epsilon}{\nu}) \approx 0$ ). One should know and control  $S(\omega)$  at the frequency  $E/\hbar$  for controlling the relaxation, and at low frequencies for controlling the dephasing. In what follows we will calculate the noise properties of a few typical experimental environments, and calculate how the noise couples to the qubit. In fact, these results are at the core of the choice of an optimum working points described in section 5.3: If  $S(0)$  from a specific environment is particularly destructive, e.g. in  $1/f$  charge noise, we make sure that that environment couples to the qubit in a way that is perpendicular on the Bloch sphere such that the flipless term vanishes. A lucid review of this quantum noise approach can be found in Ref.<sup>119</sup>.

Such methods for describing decoherence by averaging over semiclassical noise will generally fail whenever entanglement between system and bath becomes significant. This happens at large time scales, but also at stronger coupling beyond perturbation theory. This failure is due to the effect that under these conditions the system also has a pronounced influence on the bath, which changes its dynamics and from there acts back on the system. This is not captured if the noise is calculated for an a priori given (thermal) bath state.

The more conventional methods for describing decoherence rely on studying the reduced density matrix of the quantum system. This density matrix is obtained from the full density matrix of system and environment by tracing out the environment as described above. The reduced density matrix describes an ensemble of systems, i.e. the results obtained from it can be compared to results averaged over huge collections of quantum systems or a repeated experiment with identical initial conditions of the quantum system at each attempt (time-ensemble). The behavior of a *single* realization is *not* predicted, similar to the statistical description of quantum measurements<sup>128</sup>, see above. In most cases the dynamics of the

reduced density matrix can be described by a generalized master-equation with memory, i.e. by a linear integro-differential equation containing all the evolution in the past, which falls back onto the Liouville equation if the coupling to the bath is taken away<sup>129,130,131,132</sup>. Even the path-integral descriptions for open quantum systems developed from the 80s on have recently been cast in a master-equation form<sup>132</sup>. Master equations which are local in time are called *Markovian*<sup>133,134,135,136,137</sup>. Many approaches have been formulated within the Born approximation, which only contains the coupling to the bath in lowest, quadratic, order<sup>138</sup>. The simplest example for such a master equation is the phenomenological Bloch equation from NMR<sup>139,123</sup>, which introduces longitudinal relaxation rates (relaxation of the spin component parallel to the magnetic field, corresponding to energy relaxation) and transversal rates corresponding to dephasing. These equations have first been phenomenologically introduced in the picture of classical spins without having decoherence in mind. They have been further developed in NMR and can be microscopically<sup>140,123</sup> derived under suitable Markov assumptions.

There are other methods to describe open quantum systems, many of which are essentially numerical: The quantum jump or trajectory method<sup>141,142</sup> and the Bayesian formalism<sup>143</sup> rely on additional assumptions and have the advantage that they stay within a wave function representation, which is advantageous for huge systems. Various renormalization group approaches<sup>144,145,146</sup> on the other hand are very precise and include the regime of large coupling; however, up to now they have difficulties in treating nonequilibrium or driven situations.

## 7.2. Heat bath environments

So far we have given a number of examples for baths which are physically quite different, but have not detailed how to model them. It turns out that many baths can be modelled using a few general models: In the thermodynamic limit at equilibrium whenever the central limit theorem holds, systems are *Gaussian*, i.e. the distribution of values for collective variables  $X$  is of Gaussian form and can be fully described by the two-time correlation function  $\langle X(t)X(0) \rangle$ . All higher cumulants are zero. Such Gaussian models can be universally described as a bath of harmonic oscillators, and collective variables can be written as a linear combination of the oscillator coordinates<sup>67,92,132</sup>. In order to determine the appropriate couplings and distribution of the oscillators one introduces a spectral density  $J(\omega)$  of the

oscillators which is determined from the specific properties of the model under consideration. This matching to the physical model is usually done by comparing either the classical friction induced by the environment, or the noise correlation function, and will be detailed later on. Then the model of system plus bath with the appropriate  $J(\omega)$  can be solved quantum-mechanically as described above.

Oscillator bath models work well e.g. for phonon and photon baths such as electromagnetic noise. In the latter case, the (hard-core) bosons of the environment are electron-hole pairs. In many cases, the hard-core correction does not play any role and is of measure zero in the thermodynamic limit. For superconducting qubits of many kinds, the environmental spectral function  $J(\omega)$  can be readily determined from either the *noise* or the *classical friction* induced by the environment. We would like to illustrate this procedure now for the case of flux qubits.

Any linear electromagnetic environment can be described by an effective impedance  $Z_{\text{eff}}$ . If the circuit contains Josephson junctions below their critical current, they can be included through their kinetic inductance  $L_{\text{kin}} = \Phi_0 / (2\pi I_c \cos \bar{\phi})$  (see section 3), where  $\bar{\phi}$  is the average phase drop across the junction. The circuitry disturbs the qubit through its Johnson-Nyquist noise, which has Gaussian statistics and can thus be described by an effective Spin-Boson model<sup>92</sup>. In this model, the properties of the oscillator bath which forms the environment are characterized through a spectral function  $J(\omega)$ , which can be derived from the external impedance. To stay within an all-electrical analogy: We replace the resistors in the setup by infinite  $LC$  lines and perform a normal mode transformation to decouple all oscillators. Note, that other nonlinear elements such as tunnel junctions which can produce non-Gaussian shot noise are generically *not* covered by oscillator bath models.

As explained above, the flux noise from an external circuit leads to  $\epsilon = \epsilon_0 + \delta\epsilon(t)$ . For being able to treat system-bath entanglement, we write out a phenomenological Hamiltonian, the spin boson model,

$$H_{SB} = \frac{\epsilon}{2} \hat{\sigma}_z + \frac{\Delta}{2} \hat{\sigma}_x + \frac{1}{2} \hat{\sigma}_z \sum_i \lambda_i (a_i + a_i^\dagger) + \sum_i a_i^\dagger a_i \quad (14)$$

We again parametrize the noise  $\delta\epsilon(t)$  by its semiclassical power spectrum

$$S(\omega) = \langle \{ \delta\epsilon(t), \delta\epsilon(0) \} \rangle_\omega = \hbar^2 J(\omega) \coth(\hbar\omega/2k_B T). \quad (15)$$

Here,  $J(\omega)$  is formally defined as  $J(\omega) = \sum_i \lambda_i^2 \delta(\omega - \omega_i)$ . We will explain how  $J(\omega)$  can be obtained for electromagnetic environments in section

7.3. Firstly, we would like to outline an alternative approach pioneered by Leggett<sup>147</sup>, where  $J(\omega)$  is derived from the classical friction induced by the environment. In reality, the combined system of SQUID and qubit will experience fluctuations arising from additional circuit elements at different temperatures, which can be treated in a rather straightforward manner.

### 7.3. Decoherence due to the Electromagnetic Environment

#### 7.3.1. Characterizing the Environment from Classical Friction

We study a DC-SQUID in an electrical circuit as shown in Fig. 3. It contains two Josephson junctions with phase drops denoted by  $\gamma_{1/2}$ . We start by looking at the average phase  $\gamma_{\text{ex}} = (\gamma_1 + \gamma_2)/2$  across the read-out SQUID. Starting from the generalization of the RCSJ model to arbitrary shunt admittances  $Y$ , we find the equation of motion

$$2C_J \frac{\Phi_0}{2\pi} \dot{\gamma}_{\text{ex}} = -2I_{c,0} \cos(\gamma_i) \sin \gamma_{\text{ex}} + I_{\text{bias}} - \frac{\Phi_0}{2\pi} \int dt' \dot{\gamma}_{\text{ex}}(t') Y(t-t'). \quad (16)$$

Here,  $\gamma_{\text{in}} = (\gamma_1 - \gamma_2)/2$  is the dynamical variable describing the circulating current in the loop which is controlled by the flux,  $I_{\text{bias}}$  is the bias current imposed by the source,  $Y(\omega) = Z^{-1}(\omega)$  is the admittance in parallel to the whole SQUID and  $Y(\tau)$  its Fourier transform. The SQUID is described by the junction critical currents  $I_{c,0}$  which are assumed to be equal, and their capacitances  $C_J$ . We now proceed by finding a static solution which sets the operation point  $\gamma_{\text{in/ex},0}$  and small fluctuations around them,  $\delta\gamma_{\text{in/ex}}$ . The static solution reads  $I_{\text{bias}} = I_{c,\text{eff}} \sin \gamma_{\text{ex},0}$  where  $I_{c,\text{eff}} = 2I_{c,0} \cos \gamma_{\text{in},0}$  is the effective critical current of the SQUID. Linearizing Eq. (16) around this solution and Fourier-transforming, we find that

$$\delta\gamma_{\text{ex}}(\omega) = \frac{2\pi I_b \tan \gamma_{\text{in},0} Z_{\text{eff}}(\omega)}{i\omega\Phi_0} \delta\gamma_i(\omega) \quad (17)$$

where  $Z_{\text{eff}}(\omega) = (Z(\omega)^{-1} + 2i\omega C_J + (i\omega L_{\text{kin}})^{-1})^{-1}$  is the effective impedance of the parallel circuit consisting of the  $Z(\omega)$ , the kinetic inductance of the SQUID and the capacitance of its junctions. Neglecting self-inductance of the SQUID and the (high-frequency) internal plasma mode, we can straightforwardly substitute  $\gamma_{\text{in}} = \pi\Phi/\Phi_0$  and split it into  $\gamma_{\text{in},0} = \pi\Phi_{x,S}/\Phi_0$  set by the externally applied flux  $\Phi_{x,S}$  through the SQUID loop and  $\delta\gamma_i = \pi M_{\text{SQ}} I_Q/\Phi_0$  where  $M_{\text{SQ}}$  is the mutual inductance between qubit and the SQUID and  $I_Q(\vec{\varphi})$  is the circulating current in the qubit as a function of the junction phases, which assumes values  $\pm I_p$  in the classically stable states.

In order to analyze the backaction noise of the SQUID onto the qubit in the two-state approximation, we have to get back to its full, continuous description we started out from in section 5.2, the classical dynamics. These are equivalent to a particle, whose coordinates are the two independent junction phases in the three-junction loop, in a two-dimensional potential

$$\vec{C}(\Phi_0/2\pi)^2 \ddot{\vec{\varphi}} = -\nabla U(\vec{\varphi}, \Phi_{x,q} + I_S M_{\text{SQ}}). \quad (18)$$

The details of this equation are explained in Ref. <sup>73</sup> and in section 5.2.  $\vec{C}$  is the capacitance matrix describing the charging of the Josephson junctions in the loop,  $U(\vec{\varphi})$  contains the Josephson energies of the junctions as a function of the junction phases and  $I_S$  is the circulating current in the SQUID loop. The applied flux through the qubit  $\Phi_q$  is split into the flux from the external coil  $\Phi_{x,q}$  and the contribution from the SQUID. Using the above relations we find

$$I_S M_{\text{SQ}} = \delta\Phi_{\text{cl}} - 2\pi^2 M_{\text{SQ}}^2 I_B^2 \tan^2 \gamma_{\text{in},0} \frac{Z_{\text{eff}}}{i\omega\Phi_0^2} I_Q \quad (19)$$

where  $\delta\Phi_{\text{cl}} \simeq M_{\text{SQ}} I_{c,0} \cos \gamma_{\text{ex},0} \sin \gamma_{\text{in},0}$  is the non-fluctuating back-action from the SQUID.

From the two-dimensional problem, we can now restrict ourselves to the one-dimensional subspace defined by the preferred tunneling direction shown in Fig. 4 <sup>73</sup>, which is described by an effective phase  $\varphi$ . The potential restricted on this direction,  $U_{1\text{D}}(\varphi)$  has the form of a double well <sup>92,132</sup> with stable minima situated at  $\pm\varphi_0$ . In this way, we can expand  $U_{1\text{D}}(\varphi, \Phi_q) \simeq U(\varphi, \Phi_q, x) + I_Q(\varphi) I_Q M_{\text{SQ}}$ . Approximating the phase-dependence of the circulating current as  $I_Q(\varphi) \approx I_p \varphi / \varphi_0$  where  $I_p$  is the circulating current in one of the stable minima of  $\varphi$ , we end up with the classical equation of motion of the qubit including the backaction and the friction induced from the SQUID

$$\begin{aligned} & \left[ -C_{\text{eff}} \left( \frac{\Phi_0}{2\pi} \right)^2 \omega^2 + 2\pi^2 M_{\text{SQ}}^2 I_{\text{bias}}^2 \tan^2 \gamma_{\text{in},0} \frac{Z_{\text{eff}} I_p^2}{i\varphi_0 \omega \Phi_0^2} \right] \varphi \\ & = -\partial_\varphi U_{1\text{D}}(\varphi, \Phi_{x,q} + \delta\Phi_{\text{cl}}). \end{aligned} \quad (20)$$

We encode this form using the Fourier transform of the differential operators as  $D(\omega)\varphi(\omega) = -\partial U/\partial\varphi$ . We can use the prescription given in <sup>147</sup> and identify the spectral function for the continuous, classical model as  $J_{\text{cont}} = \text{Im}D(\omega)$ . From there, we can do the two-state approximation for the particle in a double well <sup>132</sup> and find  $J(\omega) = J_{\text{cont}}$  in analogy to <sup>148</sup>

$$J(\omega) = \frac{(2\pi)^2}{\hbar\omega} \left( \frac{M_{\text{SQ}} I_p}{\Phi_0} \right)^2 I_{\text{bias}}^2 \tan^2 \left( \frac{\pi\Phi}{\Phi_0} \right) \text{Re}\{Z_{\text{eff}}(\omega)\}. \quad (21)$$

This equation has a remarkable consequence: It predicts a well-defined "off"-state at  $I_{\text{bias}} = 0$ , i.e. as for any good detector, the backaction can be switched off in order to prevent the Zeno effect. In practice, one has to take into account the double-layer structure, so either the preferred working point is at finite current, or the double layer is shorted by a fourth junction<sup>90</sup>, see also section 5.3.

Note that, even though we have assumed a shunt only across the whole device, this method can be extended to describe shunts at the individual SQUID junctions as well<sup>149</sup>.

#### 7.4. Qubit Dynamics under the Influence of Decoherence

From  $J(\omega)$ , we can analyze the dynamics of the system by studying the reduced density matrix, i.e. the density matrix of the full system where the details of the environment have been integrated out, by a number of different methods. The low damping limit,  $J(\omega)/\omega \ll 1$  for all frequencies, is most desirable for quantum computation. Thus, the energy-eigenstates of the qubit Hamiltonian are the appropriate starting point of our discussion. In this case, the relaxation rate  $\Gamma_r$  (and relaxation time  $\tau_r$ ) are determined by the environmental spectral function  $J(\omega)$  at the frequency of the level separation  $E$  of the qubit by equations(12) and (13), These expressions have been derived in the context of NMR<sup>127</sup> and recently been confirmed by a full path-integral analysis<sup>124</sup>.

For performing efficient measurement, one can afford to go to the strong damping regime. A well-known approach to this problem, the noninteracting blip approximation (NIBA) has been derived in Ref.<sup>92</sup>. This approximation gives good predictions at degeneracy,  $\epsilon = 0$ . At low  $|\epsilon| > 0$  it contains an artifact predicting incoherent dynamics even at weak damping. At high bias,  $\epsilon \gg \Delta$  and at strong damping, it becomes asymptotically correct again. We will not detail this approach here more, as it has been extensively covered in<sup>92,132</sup>.

If  $J(\omega)$  is not smooth but contains strong peaks the situation becomes more involved: At some frequencies,  $J(\omega)$  may fall in the weak and at others in the strong damping limit. In some cases, where  $J(\omega) \ll \omega$  holds at least for  $\omega \leq \Omega$  with some  $\Omega \gg \nu/\hbar$ , this can be treated approximately: one can first renormalize  $\Delta_{\text{eff}}$  through the high-frequency contributions<sup>92</sup> and then perform a weak-damping approximation from the fixed-point Hamiltonian. This is detailed in Ref.<sup>150</sup>. In the general case, more involved methods such as flow equation renormalization<sup>151,152</sup>, QUAPI<sup>153</sup> or the complex

environments<sup>154</sup> approach have to be used.

### 7.5. Application: Engineering the Measurement Apparatus

From Eq. (21) we see that engineering the decoherence induced by the measurement apparatus essentially means engineering  $Z_{\text{eff}}$ . We specifically focus on the contributions due to the measurement apparatus. In this section, we are going to outline and compare several options suggested in literature. We assume a perfect current source that ramps the bias current  $I_{\text{bias}}$  through the SQUID. The fact that the current source is non-ideal, and that the wiring to the SQUID chip has an impedance is all modeled by the impedance  $Z(\omega)$ . The wiring can be engineered such that for a very wide frequency range the impedance  $Z(\omega)$  is on the order of the vacuum impedance, and can be modeled by its real part  $R_l$ . It typically has a value of 100  $\Omega$ .

It has been suggested<sup>30</sup> to overdamp the SQUID by making the shunt circuit a simple resistor  $Z(\omega) = R_S$  with  $R_S \ll \sqrt{L_{\text{kin}}/2C_J}$ . This is inspired by an analogous setup for charge qubits,<sup>155</sup>. Following the parameters given in<sup>148</sup>, we find  $\alpha R = 0.08\Omega$  and  $\omega_{\text{LR}}/R = 8.3\text{GHz}/\Omega$ .

Next, we consider a large superconducting capacitive shunt (Fig. 15a, as implemented in Refs.<sup>75,156</sup>). The  $C$  shunt only makes the effective mass of the SQUID's external phase  $\gamma_{\text{ex}}$  very heavy. The total impedance  $Z_{\text{eff}}(\omega)$  and  $J(\omega)$  are modeled as before, see Fig. 16. As limiting values, we find

$$\text{Re}\{Z_{\text{eff}}(\omega)\} \approx \begin{cases} \frac{\omega^2 L_l^2}{R_l}, & \text{for } \omega \ll \omega_{LC} \\ R_l, & \text{for } \omega = \omega_{LC} \\ \frac{1}{\omega^2 C_{sh}^2 R_l}, & \text{for } \omega \gg \omega_{LC} \end{cases} \quad (22)$$

We can observe that this circuit is a weakly damped  $LC$ -oscillator and it is clear from (12) and (21) that one should keep its resonance frequency  $\omega_{LC} = 1/\sqrt{L_J C_{sh}}$ , where  $\text{Re}\{Z_{\text{eff}}(\omega)\}$  has a maximum, away from the qubit's resonance  $\omega_{\text{res}} = \nu/\hbar$ . This is usually done by choosing  $\omega_{LC} \ll \omega_{\text{res}}$ . For a  $C$ -shunted circuit with  $\omega_{LC} \ll \omega_{\text{res}}$ , this yields for  $J(\omega \approx \omega_{LC})$

$$J(\omega) \approx \frac{(2\pi)^2}{\hbar\omega^3} \left(\frac{MI_p}{\Phi_0}\right)^2 I_{\text{bias}}^2 \tan^2\left(\frac{\pi\Phi}{\Phi_0}\right) \frac{1}{C_{sh}^2 R_l} \quad (23)$$

One has to be aware of the fact that at these high switching current values the linearization of the junction as a kinetic inductor may underestimate the actual noise. In that regime, phase diffusion between different minima of the washboard potential also becomes relevant and changes the noise

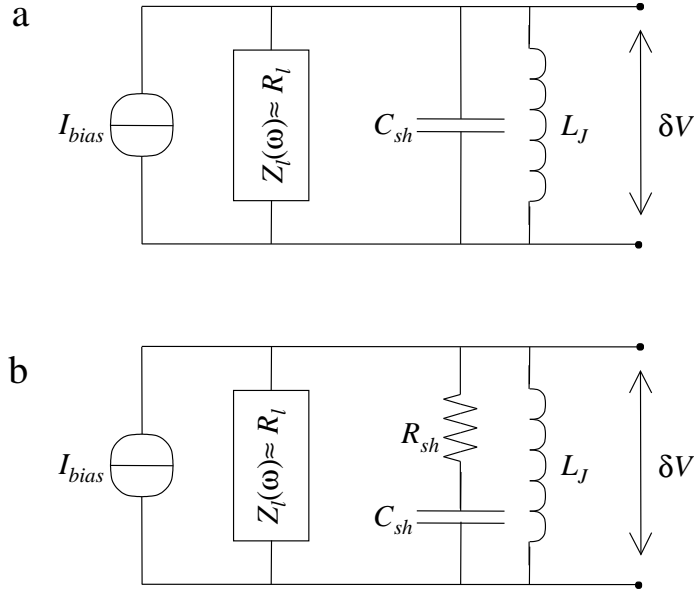


Figure 15. Circuit models for the  $C$ -shunted DC-SQUID (a) and the  $RC$ -shunted DC-SQUID (b). The SQUID is modeled as an inductance  $L_J$ . A shunt circuit, the superconducting capacitor  $C_{sh}$  or the  $R_{sh}$ - $C_{sh}$  series, is fabricated on chip very close to the SQUID. The noise that couples to the qubit results from Johnson-Nyquist voltage noise  $\delta V$  from the circuit's total impedance  $Z_{\text{eff}}$ .  $Z_{\text{eff}}$  is formed by a parallel combination of the impedances of the leads  $Z_l$ , the shunt and the SQUID, such that  $Z_{\text{eff}}^{-1} = 1/Z_l + 1/(R_{sh} + 1/i\omega C_{sh}) + 1/i\omega L_J$ , with  $R_{sh} = 0$  for the circuit (a)

properties<sup>157,158</sup>. As a complementary perspective, the  $C$ -shunted SQUID can be seen as a, generally nonlinear, cavity with small leakage rate<sup>109,154</sup>.

As an alternative we will consider a shunt that is a series combination of a capacitor and a resistor (Fig. 15b) ( $RC$ -shunted SQUID). The  $RC$  shunt also adds damping at the plasma frequency of the SQUID, which is needed for realizing a high resolution of the SQUID readout (i. e. for narrow switching-current histograms)<sup>157</sup>. The total impedance  $Z_t(\omega)$  of the two measurement circuits are modeled as in Fig. 15. For the circuit with the

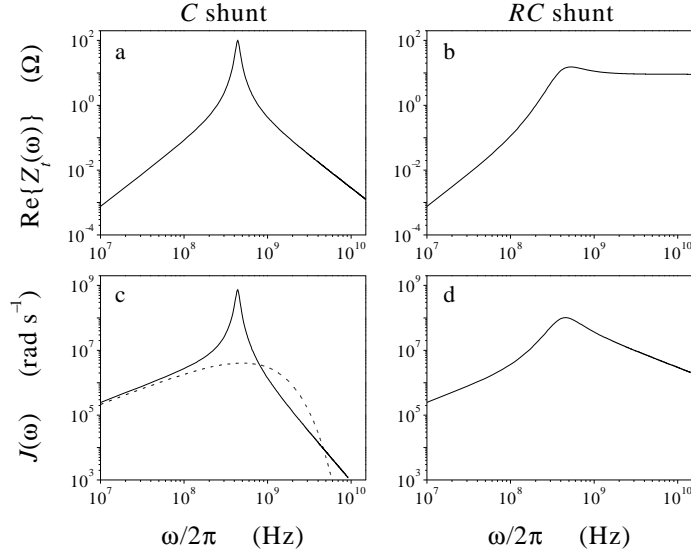


Figure 16. A typical  $\text{Re}\{Z_t(\omega)\}$  for the  $C$ -shunted SQUID (a) and the  $RC$ -shunted SQUID (b), and corresponding  $J(\omega)$  in (c) and (d) respectively. For comparison, the dashed line in (c) shows a simple Ohmic spectrum,  $J(\omega) = \alpha\omega$  with exponential cut off  $\omega_c/2\pi = 0.5$  GHz and  $\alpha = 0.00062$ . The parameters used here are  $I_p = 500$  nA and  $T = 30$  mK. The SQUID with  $2I_{co} = 200$  nA is operated at  $f = 0.75\pi$  and current biased at 120 nA, a typical value for switching of the  $C$ -shunted circuit (the  $RC$ -shunted circuit switches at higher current values). The mutual inductance  $M = 8$  pH (i. e.  $MI_p/\Phi_0 = 0.002$ ). The shunt is  $C_{sh} = 30$  pF and for the  $RC$  shunt  $R_{sh} = 10$   $\Omega$ . The leads are modeled by  $R_l = 100$   $\Omega$

$RC$  shunt

$$\text{Re}\{Z_t(\omega)\} \approx \begin{cases} \frac{\omega^2 L_l^2}{R_l}, & \text{for } \omega \ll \omega_{LC} \\ \leq R_l, & \text{for } \omega = \omega_{LC} \ll \frac{1}{R_{sh} C_{sh}} \\ R_l // R_{sh}, & \text{for } \omega = \omega_{LC} \gg \frac{1}{R_{sh} C_{sh}} \\ R_l // R_{sh}, & \text{for } \omega \gg \omega_{LC} \end{cases} \quad (24)$$

The difference mainly concerns frequencies  $\omega > \omega_{LC}$ , where the  $C$ -shunted circuit has a stronger cutoff in  $\text{Re}\{Z_{\text{eff}}(\omega)\}$ , and thereby a relaxation rate, that is several orders lower than for the  $RC$ -shunted circuit. Given the values of  $J(\omega)$  from Fig. 16, one can directly see that an  $RC$ -shunted circuit with otherwise similar parameters yields at  $\omega_{res}/2\pi = 10$  GHz relaxation times that are about four orders of magnitude shorter.

Let us remark that a different parameter regime of the  $RC$  shunt has been studied in Ref. <sup>149</sup>. Here, the  $RC$  shunts are higher in resistance and

allow to enter the quantum tunneling regime for the SQUID. Also, they are not applied across the device, but to the individual junctions. The steering of the minimum width and the histograms has been studied in great detail and good agreement between theory and experiment has been obtained. However, it turned out that the best device performance will be achieved for  $R = 0$ , a pure  $C$ -shunt.

### 7.6. *Discrete noise*

Not all environments can be described this way. A prominent counterexample are localized modes with a bounded spectrum such as spins<sup>159</sup> and structural fluctuations generating classical telegraph noise<sup>160,161,162,163</sup>, which are inherently non-Gaussian. One expects from the central limit theorem, that large ensembles of such fluctuators usually behave Gaussian again<sup>164,122</sup>, but details of this transition are only partially understood at present<sup>161,165</sup>.

Most research has concentrated on decoupling devices from external noise sources such as electromagnetic noise generated by control and measurement apparatus<sup>148</sup>. On the other hand, there inevitably are internal noise sources because the fabrication of gates, tunnel junctions, and other functional components creates defects in the underlying crystal. Prominent examples of such defects are background charges in charge-based devices or critical current fluctuations in flux-based devices<sup>166,167</sup>. A clear signature of such defects is telegraph noise in the case of a few defects or  $1/f$ -noise in the case of a larger ensemble<sup>168</sup>. With the growing success in engineering the electromagnetic environment, these defects are becoming more and more the key limiting sources of decoherence.

Such defects do not fall in the large class of noise sources that can be approximated well as a bosonic bath, and this fact complicates their analysis. Localized noise sources with bounded spectra like the defects in which we are interested produce noise that is significantly non-Gaussian. Theories treating large ensembles of non-Gaussian noise sources have been presented<sup>160,159</sup>. However, with the ongoing improvement in nanofabrication technology, it is realistic to consider the case where non-Gaussian noise sources are reduced down to only a single one or a few per device. This is the case we treat here, and thus the defects find a more realistic representation as a small set of bistable fluctuators (henceforth abbreviated bfls). In principle, this approach can be extended to larger sets of bfls with a range of different mean switching times (*e.g.*, an ensemble with an exponential distribution

of switching times that produces  $1/f$ -noise<sup>96,165,163</sup>).

### 7.7. Model of the bistable fluctuator in its semiclassical limit

We describe the bfl-noise influenced evolution of the qubit in its semiclassical limit by using a stochastic Schrödinger equation<sup>169,170</sup> with the time-dependent effective Hamiltonian

$$H_q^{\text{eff}}(t) = H_q + H_{\text{noise}}(t) \quad (25)$$

$$H_q = \hbar\epsilon_q\hat{\sigma}_z^q + \hbar\Delta_q\hat{\sigma}_x^q \quad (26)$$

$$H_{\text{noise}}(t) = \hbar\alpha\hat{\sigma}_z^q\xi_{\text{bfl}}(t) \quad (27)$$

where  $\epsilon_q$  and  $\Delta_q$  define the free (noiseless) qubit dynamics.  $\xi_{\text{bfl}}(t)$  denotes a function randomly switching between  $\pm 1$  (see Fig. 17), which represents a telegraph noise signal. The switching events follow a symmetrical Poisson process, *i.e.*, the probabilities of the bfl switching from  $+1$  to  $-1$  or  $-1$  to  $+1$  are the same and equal in time. The Poisson process is characterized by the mean time separation  $\tau_{\text{bfl}}$  between two bfl flips. The coupling amplitude to the qubit in frequency units is  $\alpha$ .

Starting with an arbitrary initial state of the qubit, represented by some given point on the Bloch sphere, we can numerically integrate the corresponding stochastic differential equation and obtain the corresponding random walk on the Bloch sphere

$$\vec{\sigma}(t) = T \exp\left(-i/\hbar \int_0^t H_q^{\text{eff}}(s) ds\right) \vec{\sigma}(0) \quad (28)$$

with  $T$  denoting the usual time-ordering operator.

### 7.8. Bang-bang control protocol

We propose to reduce the influence of the bfl-noise by applying to the qubit a continuous train of  $\pi$ -pulses along the  $\sigma_x$ -axis. This refocusing pulse scheme essentially corresponds to the standard quantum bang-bang procedure<sup>171,172,173</sup> or the Carr-Purcell-Gill-Meiboom echo technique from NMR<sup>174</sup>. For technical convenience, we consider the  $\pi$ -pulses to be of infinitesimal duration. This simplification is not crucial as described in<sup>175</sup>. The pulses are assumed to be separated by a constant time interval  $\tau_{\text{bb}}$ . The mean separation  $\tau_{\text{bfl}}$  between two bfl flips is assumed to be much longer than  $\tau_{\text{bb}}$ . For theoretical convenience, we also assume that  $\tau_{\text{bfl}}$  is shorter than

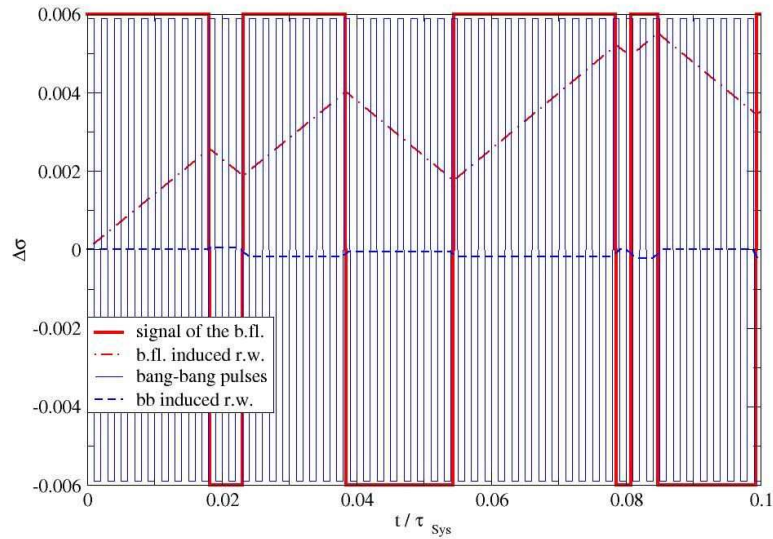


Figure 17. Schematic plot of a typical Poissonian bfl noise signal and its resulting random walk behavior (in the limit of small deviations). The periodic fast switching step function represents a bang-bang pulse with a time scale ratio:  $\tau_{\text{bfl}}/\tau_{\text{bb}} = 10$  and yields a quite smaller random walk step-length.  $\tau_{\text{Sys}} = \frac{\pi}{\sqrt{\epsilon_q^2 + \Delta_q^2}}$  denotes the evolution period of the qubit in the noiseless case.

the free precession period of the qubit. This too is not a crucial restriction. (It can always be overcome by changing to a co-precessing frame.)

Qualitatively, bang-bang control works as follows. Since  $\tau_{\text{bb}} \ll \tau_{\text{bfl}}$ , it is usually the case that the bfl does not flip during the time between two bang-bang pulses that flip the qubit. In this way, the bang-bang pulses average out the influence of  $H_{\text{noise}}(t)$ . In fact, the refocusing scheme fully suppresses the  $\sigma_z$ -term of the static Hamiltonian (26 (compare Fig. 21); but this turns out to be no crucial obstacle to universal quantum computation. As one can visualize in Fig. 17, it is only when a bfl flip occurs during a bang-bang period that the net influence of the bfl felt by the qubit is nonzero, and the qubit thus suffers some random deviation from its trajectory in the noiseless case. Taken together, these random deviations constitute a random walk around the noiseless trajectory. While this walk is actually continuous, it

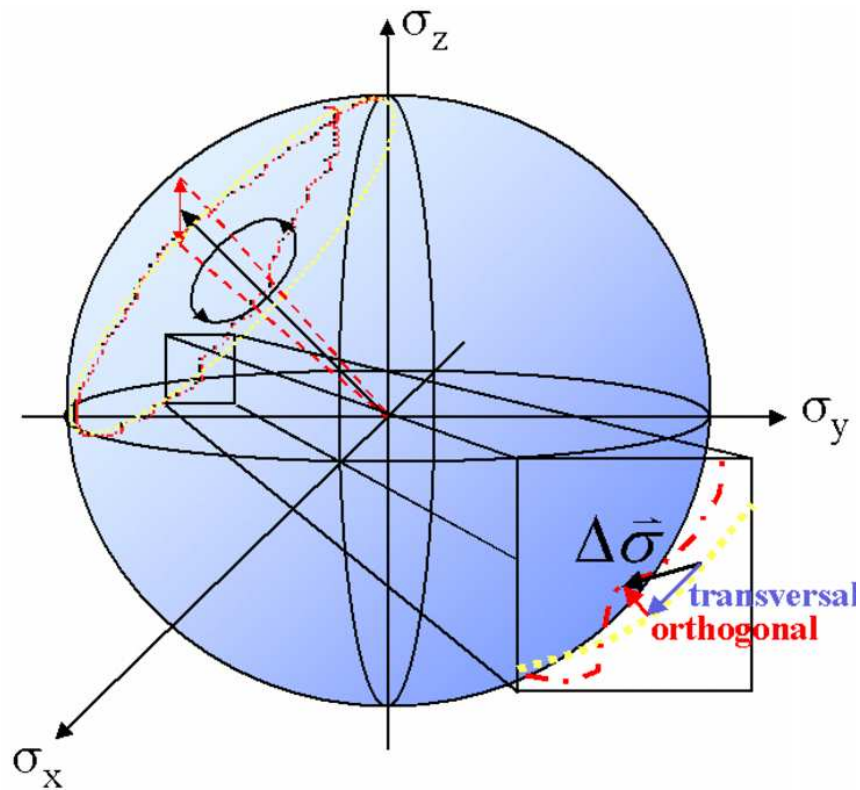


Figure 18. Schematic plot of noisy qubit evolution generated by Poissonian telegraph noise. The resulting random walk (dot-dashed line) on the Bloch sphere is comprised both of deviations  $\Delta\sigma_{\text{deph}}$  in parallel to the free precession trajectory (dotted line), which correspond to dephasing, and deviations  $\Delta\sigma_{\text{rel}}$  perpendicular to it, which correspond to relaxation/excitation.

can be modelled as a discrete walk with steps that are randomly distributed in time, one step for each bfl flip (see *e.g.* <sup>176</sup>). The average step length is essentially the product of the noise coupling strength  $\alpha$  and the mean time the bfl in its present state can influence the qubit. Without bang-bang control, this mean influence time is  $\tau_{\text{bfl}}$ , whereas with bang-bang control, it is reduced to  $\tau_{\text{bb}}$ . Therefore, both with and without bang-bang control, the random walk has the same time distribution of steps, but with bang-bang control the step size can be significantly reduced roughly by a factor of the ratio of time scales  $\tau_{\text{bb}}/\tau_{\text{bfl}}$ .

### 7.9. Random Walk on the Bloch sphere

Now we study this proposal quantitatively. We simulate these random walks both with and without bang-bang control by integrating both numerically and analytically the Schrödinger equation, Eq. (28), with the stochastic Hamiltonian of Eqs. (25-27). As generic conditions for the qubit dynamics, we choose  $\epsilon_q = \Delta_q \equiv \Omega_0$ . Without loss of generality, we set the qubit's initial state to be spin-up along the  $z$ -axis. If the qubit-bfl coupling  $\alpha$  were zero, then the qubit would simply precess freely on the Bloch sphere around the rotation axis  $\hat{\sigma}_x^q + \hat{\sigma}_z^q$  (the dotted line in Fig. 18). Hence, we expect for a sufficiently small coupling ( $\alpha \ll \Omega_0$ ) only a slight deviation of the individual time evolution compared to the free evolution case (the dashed line in Fig. 18). For the coupling strength, we take  $\alpha = 0.1\Omega_0$ . All the following times and energies are given in units of the unperturbed system Hamiltonian, *i.e.*, our time unit  $\tau_{\text{Sys}}$  is given according the free precession time  $\pi\tau_{\text{Sys}}/\sqrt{2}$ , and our energy unit is given by  $\Delta E = \sqrt{\epsilon_q^2 + \Delta_q^2} = \sqrt{2}\Omega_0$ . The time scale ratio is taken to be  $\tau_{\text{bfl}}/\tau_{\text{bb}} = 10$  if not denoted otherwise.

This approach accounts for the essential features of our specific situation: the long correlation time of the external noise, essentially  $\tau_{\text{bfl}}$ , its non-Gaussian statistics and its potentially large amplitude at low frequencies. These properties are crucial and are difficult, although not impossible, to take into account in standard master equation methods.

#### 7.9.1. Numerical simulations

We have numerically integrated Eq. (28) and averaged the deviations of the random walk evolution from the unperturbed trajectories for times up to  $100\tau_{\text{Sys}}$  over  $N = 10^3$  realizations. Larger simulations have proven that convergence is already sufficient at this stage. We shall examine the root-mean-square (rms) deviations of this ensemble at given time points

$$\Delta\vec{\sigma}_{\text{rms}}(t) = \sqrt{\frac{1}{N} \sum_{j=1}^N \left( \vec{\sigma}_j^q(t) - \vec{\sigma}_{\text{noisy},j}^q(t) \right)^2} \quad (29)$$

with and without bang-bang control. In other approaches, such as those based on master equations, one separates dephasing and relaxation. Both are contained here in Eq. (29). We shall point out notable differences between these two channels. The deviation as a function of time is plotted in Fig. 19.

The total deviations on intermediate time scales are suppressed by a

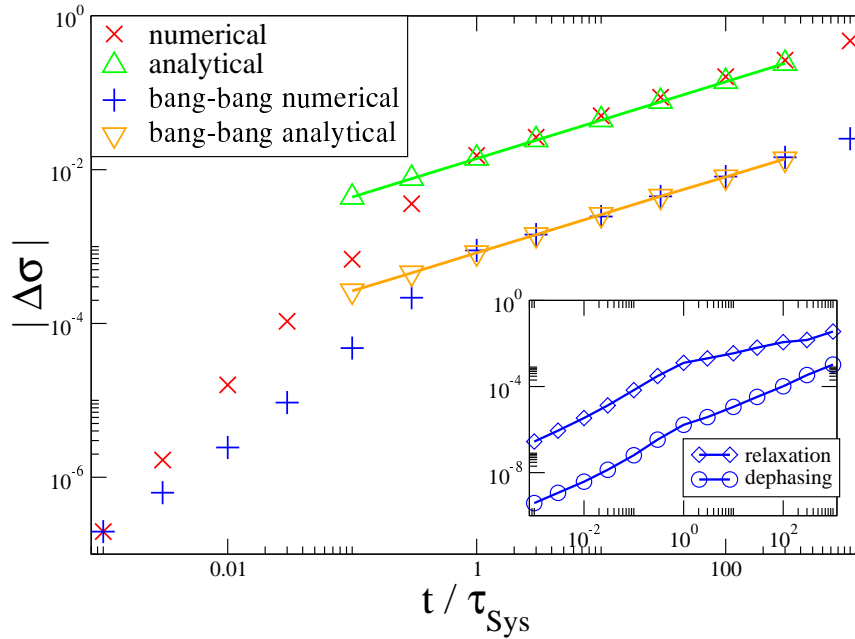


Figure 19. Time evolution of the rms deviations for bff-induced random walks with and without bang-bang control at a coupling constant  $\alpha = 0.1$  and a typical flipping time scale  $\tau_{\text{bff}} = 10^{-2}\tau_{\text{Sys}}$ . The separation between two bang-bang pulses is  $\tau_{\text{bb}} = 10^{-3}\tau_{\text{Sys}}$ . The straight lines are square-root fits of the analytical derived random walk model variances (plotted as triangles). Inset: Components of the deviations from the free precession trajectory that are parallel to it (dephasing) and perpendicular to it (relaxation/excitation) with bang-bang control.

ratio on the order of 10. A detailed numerical analysis shows that *without* bang-bang suppression, the deviations parallel to the free precession trajectory (which correspond to dephasing) are of similar size to those perpendicular to free precession (which correspond to relaxation/excitation). In contrast, with bang-bang control, dephasing is almost totally absent as one can see in the inset of Fig. 19.

The main double-logarithmic plot of Fig. 19 shows that on short time scales ( $t \simeq 0.1\tau_{\text{Sys}}$ , which corresponds to  $\simeq 10$  random walk steps), deviations increase almost linearly in time. It is not until times on the order of  $\tau_{\text{Sys}}$  that the noise-induced deviations start to behave as typical classical random walks, increasing as a square-root in time.

### 7.9.2. Analytical random walk models

We now develop analytical random walk models for our system. The random walk on the Bloch sphere is in general two-dimensional, consisting of both parallel and perpendicular deviations to the free evolution trajectory. Bang-bang control, as was seen in the above numerical results and as will be seen in the following analytical results, essentially reduces the random walk to one-dimension as only the perpendicular deviations remain significant. In the following, we restrict ourselves to the long-time (many random walk steps) regime.

We first calculate for both cases the probability distributions of the deviations after one bfl flip (“one-step deviations” in terms of the discrete random walk). The fluctuation of the period between  $\tau_{\text{per}}^{\pm}$  leads to dephasing, which can be evaluated at  $\alpha \ll \epsilon_q, \Delta_q$  to

$$\Delta\vec{\sigma}_{\text{deph}}^{\text{bfl}} = 2\pi \cos \phi \left( \frac{1}{\tau_{\text{per}}^{\pm}} - \frac{1}{\tau_{\text{per}}} \right) \tau_{\text{bfl}} \simeq \pm 2 \frac{\Delta_q \epsilon_q}{\Delta_q^2 + \epsilon_q^2} \alpha \tau_{\text{bfl}}. \quad (30)$$

For the relaxation/excitation effect of the noise, one has to use the projection of the perturbation orthogonal to the free axis.

In total, using  $\tau_{\text{per}}^{\pm} \simeq \tau_{\text{per}}$  to first order in  $\alpha$ , we find

$$\Delta\vec{\sigma}_{\text{rel}}^{\text{bfl}} = 2\pi \cos \phi \sin \eta \frac{1}{\sqrt{2}} \cos \phi \frac{\tau_{\text{bfl}}}{\tau_{\text{per}}^{\pm}} \simeq \sqrt{2} \frac{\Delta_q^3}{(\epsilon_q^2 + \Delta_q^2)^{3/2}} \alpha \tau_{\text{bfl}}. \quad (31)$$

The derivation of the maximal one-step deviation for the bang-bang controlled situation has to be handled differently. The deviation resulting from a bfl flip during a bang-bang pulse period is maximal if the step happens exactly at the moment of the second qubit spin-flip (*i.e.*, in the middle of the bang-bang cycle). When this happens, the refocusing evolution has in its first half a drift, for example, to the “right” (compare Fig. 21) and in the last half an equal aberration.

We average the maximal one-step deviation over one precession period in the usual rms manner to obtain

$$\begin{aligned} \langle \Delta\vec{\sigma}_{\text{max}}^{\text{bb}} \rangle &= \sqrt{\frac{1}{2\pi} \int_0^{2\pi} \sin^2 \chi 4\alpha^2 \tau_{\text{bb}}^2 d\chi} \\ &= \sqrt{2} \alpha \tau_{\text{bb}}. \end{aligned} \quad (32)$$

Obviously, this variance only contributes to relaxation.

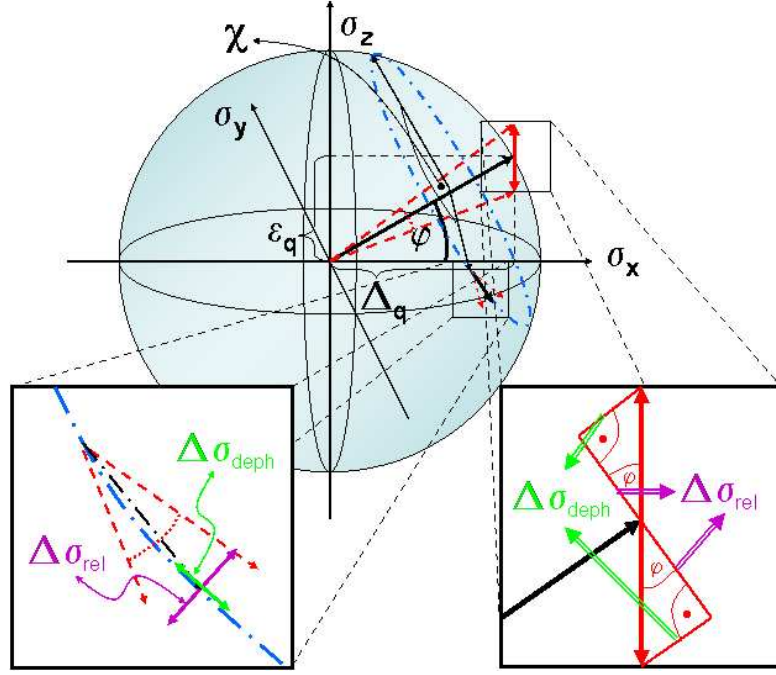


Figure 20. Plot of a typical one-step deviation from the unperturbed qubit trajectory with generic values for  $\epsilon_q$  and  $\Delta_q$ . The fractions of the bfl fluctuations in  $\hat{\sigma}_z$ -direction have to be distinguished with respect to their effects on the qubit: those that yield dephasing deviations that are parallel to the free precession trajectory (proportional to  $\sin \phi$ ) versus relaxation/excitation deviations that are perpendicular (proportional to  $\sin \eta$ ). Both parts are additionally dominated by a factor of  $\cos \phi$  due to the diminished radius of the trajectory starting from the initial state  $\sigma_z = +1$ . The impact of the relaxation/excitation generating part is furthermore depending on  $\cos \phi$  as well as  $\sin \chi$ , the azimuth angle of the qubits present position.

From the long-time limit of our analytical random walk distribution, we find for their variances in real space representation

$$\Delta\sigma_{\text{bfl}}(N_{\text{bfl}}) = \sqrt{N_{\text{bfl}}}\beta = \sqrt{N_{\text{bfl}}}\frac{\sqrt{5}}{2}\alpha\tau_{\text{bfl}} \quad (33)$$

for the case without bang-bang control and

$$\Delta\sigma_{\text{bb}}(N_{\text{bfl}}) = \frac{\sqrt{N_{\text{bfl}}}}{2}\gamma = \sqrt{\frac{N_{\text{bfl}}}{2}}\alpha\tau_{\text{bb}} \quad (34)$$

for the case with it. In the large- $N_{\text{bfl}}$  limit, this model shows excellent agreement with the numerical simulations.

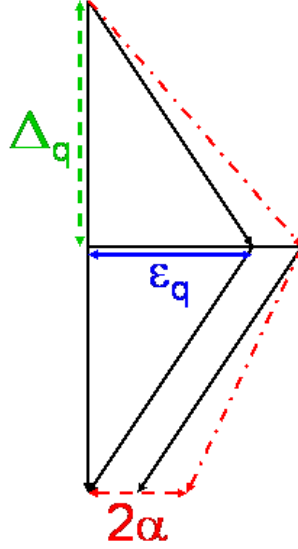


Figure 21. Sketch of a maximal one-step deviation during a bang-bang modulated cycle, which appears if the bfl state flips precisely at the intermediate bang-bang pulse time. The dephasing part of deviation evidently averages out, while a relaxing aberrance arise proportional to the noise-coupling constant  $\alpha$ .

### 7.9.3. Bang-bang control working as a high-pass filter

In order to measure the degree of noise suppression due to bang-bang control, we define the suppression factor  $\mathcal{S}_{t_0}$  as follows for a given evolution time  $t_0$

$$\mathcal{S}_{t_0}(\tau_{\text{bfl}}/\tau_{\text{bb}}) \equiv \frac{\Delta\bar{\sigma}_{\text{rms}}^{\text{bfl}}(t_0)}{\Delta\bar{\sigma}_{\text{rms}}^{\text{bb}}(t_0)}. \quad (35)$$

We now systematically study the dependence of  $\mathcal{S}_{t_0}$  on  $\tau_{\text{bfl}}/\tau_{\text{bb}}$  for a constant mean bfl switching rate  $\tau_{\text{bfl}} = 10^{-2}\tau_{\text{sys}}$  at a fixed evolution time  $t_0 = \tau_{\text{sys}}$ . The numerical data in Fig. 22 show that the suppression efficiency is linear in the bang-bang repetition rate,  $\mathcal{S}_{\tau_{\text{sys}}} = \mu\tau_{\text{bfl}}/\tau_{\text{bb}}$ . The numerically derived value of the coefficient,  $\mu_{\text{numerical}} \approx 1.679$ , is in excellent agreement with the analytical result  $\mu_{\text{analytical}} = \sqrt{5/2} \simeq 1.581$  from our saddle point approximation, Eqs. (33) and (34).

We have investigated the qubit errors that arise from the noise gener-

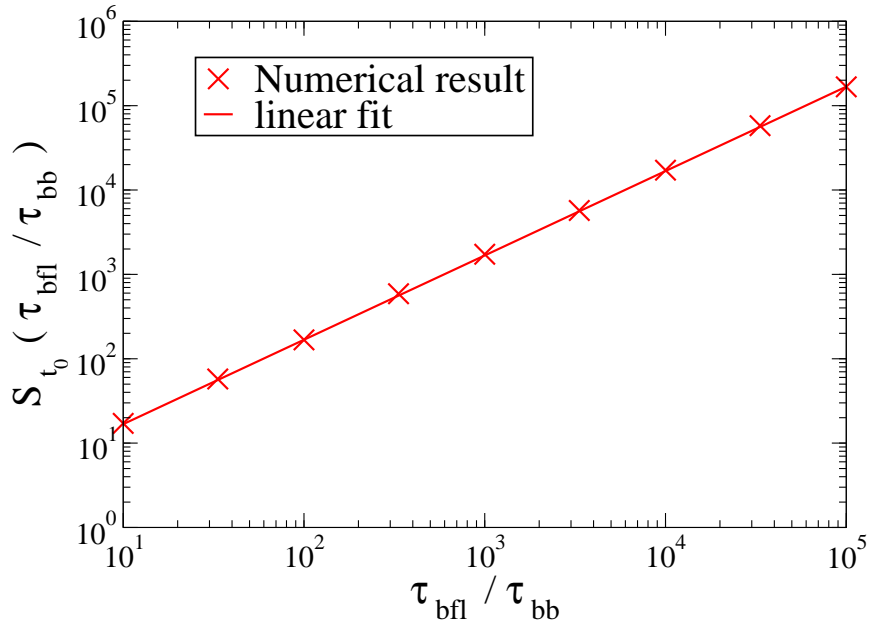


Figure 22. The suppression factor  $S_{t_0}(\tau_{bfl}/\tau_{bb}) = \frac{\Delta\sigma_{rms}^{bfl}(t_0)}{\Delta\sigma_{rms}^{bb}(t_0)}$  evaluated for  $t_0 = \tau_{Sys}$  as a function of the ratio of the mean switching time  $\tau_{bfl}$  and the bang-bang pulse separation  $\tau_{bb}$ .

ated by a *single* bistable fluctuator (bfl) in its semiclassical limit, where it behaves as a telegraph noise source. We numerically integrated a corresponding stochastic Schrödinger equation, Equ. (28), as well as analytically solved (in the long-time limit) appropriate random walk models. As a characteristic measure of the resulting dephasing and relaxation effects, we used the rms deviation of noisy evolutions compared to noiseless ones. To suppress the effects of this noise, we presented a bang-bang pulse sequence analogous to the familiar spin-echo method. We claimed this pulse sequence to be capable of refocusing most of the bfl-noise induced aberrations. Both in the case without bang-bang control and the case with it, there was excellent agreement between our numerical and analytical results on the relevant intermediate time scales (*i.e.*, times after a short initial phase where deviations grow linearly instead of as a square-root in time, but before the qubit becomes totally decohered).

Meanwhile, several other extensions of Ref. <sup>177,175</sup> have been proposed by other research groups. Ref. <sup>163</sup> includes a larger number of fluctua-

tors, described as semiclassical noise sources, but restricts itself to a single spin-echo cycle. Ref. <sup>162</sup> analyzes extensively the importance of higher, non-Gaussian cumulants and memory effects and arrives at a number of analytical results, but it does not treat the option of refocusing. Ref. <sup>178</sup> treats a full microscopic model and compares different variations of the bang-bang pulse sequence. Ref. <sup>179</sup> also treats a full microscopic model with potentially many fluctuators using a Lindblad-type approach and covers a wide range of ratios between the fluctuator and bang-bang pulse time scales. One of its main conclusions is that a Zeno effect is found in a parameter regime not covered by our work. Note that all of these other extensions of our work treat only the case of ideal bang-bang pulses.

## 8. Coupled qubits and beyond

To implement a quantum algorithm, one must be able to entangle multiple qubits, so that an interaction term is required in the Hamiltonian describing a two qubit system. For two superconducting flux qubits, the natural interaction is between the magnetic fluxes. Placing the two qubits in proximity provides a permanent coupling through their mutual inductance <sup>180</sup>. Pulse sequences for generating entanglement have been derived for several superconducting qubits with fixed interaction energies <sup>107,181</sup>. However, entangling operations can be much more efficient if the interaction can be varied and, ideally, turned off during parts of the manipulation. A variable coupling scheme for charge-based superconducting qubits with a bipolar interaction has been suggested recently <sup>182</sup>. For flux qubits, while switchable couplings have been proposed previously <sup>73,183</sup>, these approaches do not enable one to turn off the coupling entirely and require separate coupling and flux readout devices.

As a new device, we propose a new coupling scheme for flux qubits in which the interaction is adjusted by changing a relatively small current. For suitable device parameters the sign of the coupling can also be changed, thus making it possible to null out the direct interaction between the flux qubits. Furthermore, the same device can be used both to vary the coupling and to read out the flux states of the qubits. We show explicitly how this variable qubit coupling can be combined with microwave pulses to perform the quantum Controlled-NOT (CNOT) logic gate. Using microwave pulses also for arbitrary single-qubit operations, this scheme provides all the necessary ingredients for implementation of scalable universal quantum logic.

The coupling is mediated by the circulating current  $J$  in a dc Superconducting QUantum Interference Device (SQUID), in the zero voltage state, which is coupled to each of two qubits through an identical mutual inductance  $M_{qs}$  [Fig. 23(a)]. A variation in the flux applied to the SQUID,  $\Phi_s$ , changes  $J$  [Fig. 23(b)]. The response is governed by the screening parameter  $\beta_L \equiv 2LI_0/\Phi_0$  and the bias current  $I_b$ , where  $I_b < I_c(\Phi_s)$ , the critical current for which the SQUID switches out of the zero voltage state at  $T = 0$  in the absence of quantum tunneling. In flux qubit experiments<sup>75</sup>, the flux state is determined by a dc SQUID to which fast pulses of  $I_b$  are applied to measure  $I_c(\Phi_s, T)$ . Thus, existing technology allows  $I_b$  to be varied rapidly, and a single dc SQUID can be used both to measure the two qubits and to couple them together controllably.

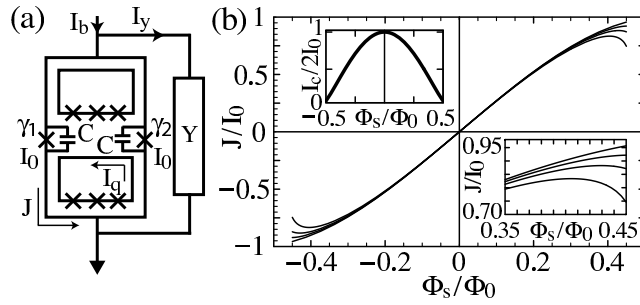


Figure 23. (a) SQUID-based coupling scheme. The admittance  $Y$  represents the SQUID bias circuitry. (b) Response of SQUID circulating current  $J$  to applied flux  $\Phi_s$  for  $\beta_L = 0.092$  and  $I_b/I_c(0.45\Phi_0) = 0, 0.4, 0.6, 0.85$  (top to bottom). Lower right inset shows  $J(\Phi_s)$  for same values of  $I_b$  near  $\Phi_s = 0.45\Phi_0$ . Upper left inset shows  $I_c$  versus  $\Phi_s$ .

The energy biases  $\epsilon_i^0$  are determined by the flux bias of each qubit relative to  $\Phi_0/2$ . The tunnel frequencies  $\delta_i/h$  are fixed by the device parameters, and are typically a few GHz. For two flux qubits, arranged so that a flux change in one qubit alters the flux in the other, the coupled-qubit Hamiltonian describing the dynamics in the complex 4-dimensional Hilbert space becomes

$$\mathcal{H} = \mathcal{H}_1 \otimes I^{(2)} + I^{(1)} \otimes \mathcal{H}_2 - (K/2)\sigma_z^{(1)} \otimes \sigma_z^{(2)}, \quad (36)$$

where  $I^{(i)}$  is the identity matrix for qubit  $i$  and  $K$  characterizes the coupling energy. For  $K < 0$ , the minimum energy configuration corresponds to anti-parallel fluxes. For two flux qubits coupled through a mutual inductance

$M_{qq}$ , the interaction energy is fixed at  $K_0 = -2M_{qq} \left| I_q^{(1)} \right| \left| I_q^{(2)} \right|$ .

For the configuration of Fig. 23(a), in addition to the direct coupling,  $K_0$ , the qubits interact by changing the current  $J$  in the SQUID. The response of  $J$  to a flux change depends strongly on  $I_b$  [Fig. 23(b)]. When  $I_q^{(2)}$  switches direction, the flux coupled to the SQUID,  $\Delta\Phi_s^{(2)}$ , induces a change  $\Delta J$  in the circulating current in the SQUID, and alters the flux coupled from the SQUID to qubit 1. The corresponding coupling is

$$K_s = I_q^{(1)} \Delta\Phi_q^{(1)} = -2M_{qs}^2 \left| I_q^{(1)} \right| \left| I_q^{(2)} \right| \operatorname{Re}(\partial J / \partial \Phi_s)_{I_b}. \quad (37)$$

The transfer function,  $(\partial J / \partial \Phi_s)_{I_b}$ , is related to the dynamic impedance,  $Z$ , of the SQUID via<sup>184</sup>

$$\partial J / \partial \Phi_s = i\omega / Z = 1/L + i\omega/R, \quad (38)$$

where  $R$  is the dynamic resistance, determined by  $Y$  which dominates any loss in the Josephson junctions, and  $L$  is the dynamic inductance which, in general, differs from the geometrical inductance of the SQUID,  $L$ .

We evaluate  $(\partial J / \partial \Phi_s)_{I_b}$  by current conservation, neglecting currents flowing through the junction resistances:

$$I_b = I_y + 2I_0 \cos \Delta\gamma \sin \bar{\gamma} - 2C(\Phi_0/2\pi)\ddot{\gamma}, \quad (39)$$

$$J = I_0 \cos \bar{\gamma} \sin \Delta\gamma - C(\Phi_0/2\pi)\Delta\ddot{\gamma}. \quad (40)$$

Here,  $I_y$  is the current flowing through the admittance  $Y(\omega)$  [Fig. 23(a)], and  $I_0$  and  $C$  are the critical current and capacitance of each SQUID junction. The phase variables are related to the phases across each junction,  $\gamma_1$  and  $\gamma_2$ , as  $\Delta\gamma = (\gamma_1 - \gamma_2)/2$  and  $\bar{\gamma} = (\gamma_1 + \gamma_2)/2$ . The phases are constrained by  $d\Delta\gamma = (\pi/\Phi_0)(d\Phi_s - LdJ)$ .

The expression for  $K_s$  in terms of  $\operatorname{Re}(\partial J / \partial \Phi_s)_{I_b}$  (Eq. 37) requires the qubit frequencies to be much lower than the characteristic frequencies of the SQUID. This condition is satisfied by our choice of device parameters, and also ensures that the SQUID stays in its ground state during qubit entangling operations. Furthermore, it is a reasonable approximation to take the  $\omega = 0$  limit of  $\operatorname{Re}(\partial J / \partial \Phi_s)_{I_b}$  to calculate  $K_s$ , so that we can solve Eqs. (39) and (40) numerically to obtain the working point; for the moment we assume  $Y(0) = 0$ . For the small deviations determining  $K_s$ , we linearize Eqs. (39) and (40) and solve for the real part of the transfer function in the low-frequency limit:

$$\operatorname{Re} \left( \frac{\partial J}{\partial \Phi_s} \right)_{I_b} = \frac{1}{2L_j} \frac{1 - \tan^2 \Delta\gamma \tan^2 \bar{\gamma}}{1 + \frac{L}{2L_j} (1 - \tan^2 \Delta\gamma \tan^2 \bar{\gamma})}. \quad (41)$$

Here, we have introduced the Josephson inductance for one junction,  $L_j = \Phi_0/2\pi I_0 \cos \Delta\gamma \cos \bar{\gamma}$ . For  $\beta_L \gg 1$ , Eq. (41) approaches  $1/L$ , while for  $\beta_L \ll 1$ ,

$$\text{Re}(\partial J/\partial \Phi_s)_{I_b} = (1/2L_j)(1 - \tan^2 \Delta\gamma \tan^2 \bar{\gamma}). \quad (42)$$

We see that  $\text{Re}(\partial J/\partial \Phi_s)_{I_b}$  becomes negative for sufficiently high values of  $I_b$  and  $\Phi_s$ , which increase  $\bar{\gamma}$  and  $\Delta\gamma$ .

We choose the experimentally-accessible SQUID parameters  $L = 200$  pH,  $C = 5$  fF, and  $I_0 = 0.48$   $\mu\text{A}$ , for which  $\beta_L = 0.092$ . The qubits are characterized by  $I_q^{(1)} = I_q^{(2)} = 0.46$   $\mu\text{A}$ ,  $M_{qs} = 33$  pH, and  $M_{qq} = 0.25$  pH, yielding  $K_0/h = -0.16$  GHz. Choosing  $\Phi_s = 0.45\Phi_0$ , Eqs. (37) and (41) result in a net coupling strength  $K/h = (K_0 + K_s)/h$  that is  $-0.3$  GHz when  $I_b = 0$ , and zero when  $I_b/I_c(0.45\Phi_0) = 0.57$  [Fig. 24(a)]. The change in sign of  $K_s$  does not occur for all  $\beta_L$ . Figure 24(b) shows the highest achievable value of  $K_s$  versus  $\beta_L$ . We have adopted the optimal design at  $\beta_L = 0.092$ .

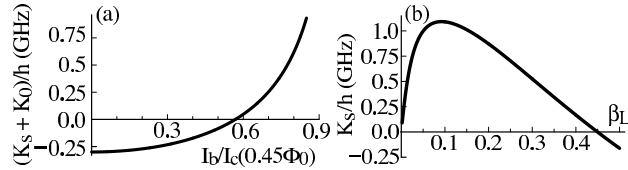


Figure 24. (a) Variation of  $K$  with  $I_b$  for  $\Phi_s = 0.45\Phi_0$  and device parameters described in text. (b) Highest achievable value of  $K_s$  versus  $\beta_L$  evaluated at  $I_b = 0.85I_c(0.45\Phi_0)$ ;  $I_0$  (and hence  $\beta_L$ ) is varied for  $L = 200$  pH.

We also need to consider crosstalk between the coupling and single-qubit terms in the Hamiltonian. When the coupling is switched, in addition to  $\partial J/\partial \Phi_s$  being altered,  $J$  also changes, thus shifting the flux biases of the qubits. The calculated change in  $J$  as the coupler is switched from  $I_b = 0$  to  $I_b/I_c(0.45\Phi_0) = 0.57$  produces a change in the flux in each qubit corresponding to an energy shift  $\delta\epsilon_1/h = \delta\epsilon_2/h = 1.64$  GHz. In addition, when the qubits are driven by microwaves to produce single-qubit rotations, the microwave flux may also couple to  $\Phi_s$ . As a result,  $K$  is weakly modulated when the coupling would nominally be turned off. A typical microwave drive  $\tilde{\epsilon}_i(t)/h$  of amplitude 1 GHz results in a variation of about  $\pm 14$  MHz about  $K = 0$ .

When the bias current is increased to switch off the coupling, the SQUID symmetry is broken and the qubits are coupled to the noise generated by

the admittance  $Y$ . We estimate the decoherence due to this process using the technique outlined in section 7.3. We obtain as an intermediate result

$$\mathcal{J}(\omega) = (I_q^2 M_{qs}^2 / h) \text{Im}(\partial J / \partial \Phi_s)_{I_b}. \quad (43)$$

For the case  $Y^{-1} = R$ , following the path to the static transfer function Eq. (41) and taking the imaginary part in the low- $\beta_L$  limit, we obtain  $\text{Im}(\partial J / \partial \Phi_s)_{I_b} = -\omega / R = (\omega / 4R) \tan^2 \Delta\gamma \tan^2 \bar{\gamma}$ . Thus  $J(\omega) = \alpha\omega$ , where  $\alpha = (M_{qs}^2 I_q^2 / 4hR) \tan^2 \Delta\gamma \tan^2 \bar{\gamma}$ , and  $\alpha(I_b = 0) = 0$ . As  $I_b$  is increased to change the coupling strength,  $\alpha$  increases monotonically. For the parameters described above and for  $R = 2.4$  k $\Omega$ , when the net coupling is zero [ $I_b / I_c(0.45\Phi_0) = 0.57$ , Fig. 24(a)], we find  $\alpha = 8 \times 10^{-5}$  corresponding to a qubit dephasing time of about 500 ns, one order of magnitude larger than values currently measured in flux qubits<sup>75</sup>, however, shorter than the best values with flux echo.

We now show that this configuration implements universal quantum logic efficiently. Any  $n$ -qubit quantum operation can be decomposed into combinations of two-qubit entangling gates, for example, CNOT, and single-qubit gates<sup>185</sup>. Single-qubit gates generate local unitary transformations in the complex 2-dimensional subspace for the corresponding individual qubit, while the two-qubit gates correspond to unitary transformations in the 4-dimensional Hilbert space. Two-qubit gates which cannot be decomposed into a product of single-qubit gates are said to be nonlocal, and may lead to entanglement between the two qubits<sup>186</sup>. Since we can adjust the qubit coupling  $K$  to zero, we can readily implement single-qubit gates with microwave pulses as described below.

To implement the nonlocal two-qubit CNOT gate, we use the concept of local equivalence: the two-qubit gates  $U_1$  and  $U_2$  are locally equivalent if  $U_1 = k_1 U_2 k_2$ , where  $k_1$  and  $k_2$  are local two-qubit gates which are combinations of single-qubit gates applied simultaneously. These unitary transformations on the two single-qubit subspaces transform the gate  $U_2$  into  $U_1$ . The local gate which precedes  $U_2$ ,  $k_2$ , is given by  $k_{21} \otimes k_{22}$ , where  $k_{21(22)}$  is a single-qubit gate for qubit 1(2), while the local gate which follows  $U_2$ ,  $k_1$ , is  $k_{11} \otimes k_{12}$ , where  $k_{11(12)}$  is a single-qubit gate for qubit 1(2)<sup>187</sup>. Our strategy is to find efficient implementation of a nonlocal quantum gate  $U_2$  that differs only by local gates,  $k_1$  and  $k_2$ , from CNOT, using the methods in<sup>186</sup>, and the computational basis, in which the SQUID measures the projection of each qubit state vector onto the z-axis.

The local equivalence classes of two-qubit operations have been shown<sup>186</sup> to be in one-to-one correspondence with points in a tetrahedron, the

Weyl chamber. In this geometric representation, any two-qubit operation is associated with the point  $[c_1, c_2, c_3]$ , where CNOT corresponds to  $[\pi/2, 0, 0]$ . Furthermore, the nonlocal two-qubit gates generated by a Hamiltonian acting for time  $t$  can be mapped to a trajectory in this space<sup>186</sup>. If  $K$  is increased instantaneously to a constant value, the trajectory generated by Eq. (36) is well described by the following periodic curve

$$[c_1, c_2, c_3] = [Kvt/\hbar, p|\sin\omega t|, p|\sin\omega t|]. \quad (44)$$

Here,  $p$  is a function of the system parameters,  $v = \epsilon_1^0\epsilon_2^0/\Delta E_1\Delta E_2$ , and  $\omega = (\Delta E_1 - \Delta E_2)/2\hbar$ , where  $\Delta E_i = [(\epsilon_i^0)^2 + \delta_i^2]^{1/2}$  is the single-qubit energy level splitting. Independently of  $p$ , this trajectory reaches  $[\pi/2, 0, 0]$  in a time  $t_K = n\pi/\omega$  when the coupling strength is tuned to  $K = \hbar\omega/2nv$ , with  $n$  a nonzero integer.

While this analytic solution contains the essential physics, it is an approximation and does not include vital experimental features, in particular, crosstalk and the finite rise time of the bias current pulse. To improve the accuracy, we perform a numerical optimization using Eq. (44) as a starting point, then add these corrections. We use tunnel frequencies  $\delta_1/h = 5$  GHz and  $\delta_2/h = 3$  GHz, and include the shifts of the single-qubit energy biases due to the crosstalk with  $K_s$  in Eq. (44) by adding a shift  $\delta\epsilon_i$  proportional to  $K$ . We account for the rise and fall times of the current pulse by using pulse edges with 90% widths of 0.5 ns [see  $K(t)$  in Fig. 25]. We numerically optimize the variable parameters to minimize the Euclidean distance between the actual achieved gate and the desired Weyl chamber target CNOT gate. We find  $K/h = -0.30$  GHz,  $\epsilon_1^0/h = 8.06$  GHz,  $\epsilon_2^0/h = 2.03$  GHz, and  $t_K = 8.74$  ns;  $t_K$  is the time during which the qubit coupling is turned on.

As outlined above, to achieve a true CNOT gate we still have to determine the pulse sequences which implement the requisite local gates that take this Weyl chamber target  $U_2$  to CNOT in the computational basis. Local gates may be implemented by applying microwave radiation,  $\tilde{\epsilon}_i(t)$ , which couples to  $\sigma_z^{(i)}$ , and is at or near resonance with the single-qubit energy level splitting  $\Delta E_i$ . We note that the single-qubit Hamiltonian driven by a resonant oscillating microwave field does not permit one to use standard NMR pulses, since the static and oscillating fields are not perpendicular, but rather are canted by an angle  $\tan^{-1}(\delta_i/\epsilon_i^0)$ . To simplify the pulse sequence, we keep  $\epsilon_{1,2}^0$  constant at the values used for the non-local gate generation. This imposes an additional constraint on the local gates: to generate a local two-qubit gate  $k_1 = k_{11} \otimes k_{12}$ , the two single-qubit gates  $k_{11}$  and  $k_{12}$  must be simultaneous and of equal duration. We satisfy this

constraint by making the microwave pulse addressing one qubit resonant and that addressing the other slightly off-resonance. Using this offset and the relative amplitude and phase of the two microwave pulses as variables, we can achieve two different single-qubit gates simultaneously, leading to our required local two-qubit gate.

The resulting pulse sequences for  $K$  and  $\tilde{\epsilon}_{1,2}$  are shown in Fig. 25. The gate has a maximum deviation from CNOT in the computational basis of 1.6% in any matrix element. This error arises predominantly from the cross-coupling of the microwave signals for the two qubits and the weak modulation of the  $K = 0$  state of the coupler during the single-qubit microwave manipulations. While small, this error could be reduced further by performing the numerical optimization with higher precision or by coupling the microwave flux selectively to each of the qubits and not to the SQUID. The total elapsed time of 29.35 ns is comparable to measured dephasing times in a single flux qubit<sup>75</sup>.

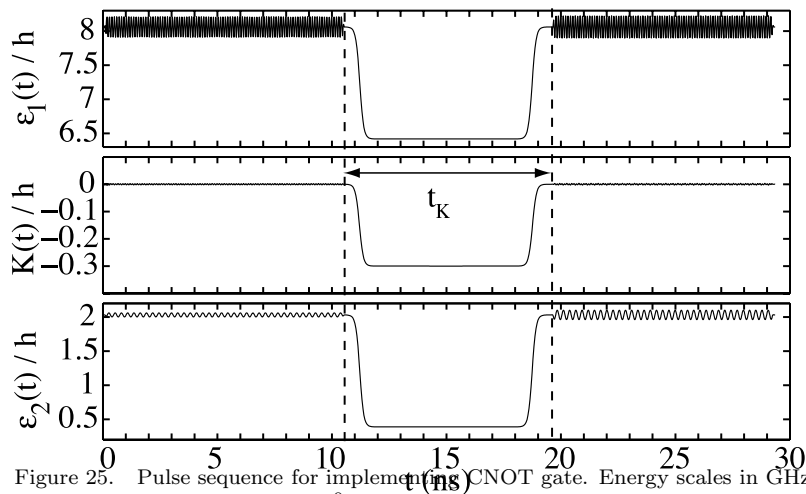


Figure 25. Pulse sequence for implementing a CNOT gate. Energy scales in GHz. Total single-qubit energy bias  $\epsilon_i(t) = \epsilon_i^0 + \tilde{\epsilon}_i(t) + \delta\epsilon_i(t)$ , where microwave pulses  $\tilde{\epsilon}_{1,2}(t)$  produce single-qubit rotations in the decoupled configuration; crosstalk modulation of  $K(t)$  is shown (see text). The bias current is pulsed to turn on the interaction in the central region.

We have shown in the preceding paragraphs that the inverse dynamic inductance of a dc SQUID with low  $\beta_L$  in the zero-voltage state can be varied by pulsing the bias current. This technique provides a variable-strength interaction  $K_s$  between flux qubits coupled to the SQUID, and

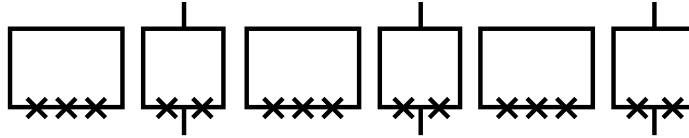


Figure 26. Chain of flux qubits with intervening dc SQUIDs arranged to provide both variable nearest neighbor coupling and qubit readout.

enables cancellation of the direct mutual inductive coupling  $K_0$  between the qubits so that the net coupling  $K$  can be switched from a substantial value to zero. By steering a nonlocal gate trajectory and combining it with local gates composed of simultaneous single-qubit rotations driven by resonant and off-resonant microwave pulses, we have shown that a simple pulse sequence containing a single switching of the flux coupling for fixed static flux biases results in a CNOT gate and full entanglement of two flux qubits on a timescale comparable to measured decoherence times for flux qubits. Furthermore, the same SQUID can be used to determine the flux state of the qubits. This approach should be readily scalable to larger numbers of qubits, as, for example, in Fig. 26.

A wide range of other coupling schemes have been proposed and a few of them realized, which we will briefly review here. We will indicate a coupling Hamiltonian of the form  $K\sigma_a \otimes \sigma_b$  simply as  $AB$ .

A constant  $ZZ$  coupling using a flux transformer has been demonstrated for flux qubits<sup>180</sup>. This is expected to be possible up to strong coupling<sup>188</sup>. This transformer can in principle be made tunable by including a DC-SQUID loop<sup>73,74</sup> or another superconducting switch<sup>189</sup> into the loop. Alternatively, the conjugate variable, charge, can be used in capacitive coupling, leading to a non-tunable  $XX + YY$  interaction<sup>190</sup>. All of these proposals need one physical coupling element per interacting pair, so they will conceivably be of nearest-neighbor type.

For phase qubits, the coupling is not straightforwardly put into a Pauli matrix representation and the coupling matrix is generally bias dependent<sup>191</sup> and also depends on whether the qubits are encoded into adiabatic eigenstates or a global basis; however, the resulting interaction certainly has entangling power<sup>181</sup>. A spectroscopic hint on two-qubit entanglement<sup>192</sup> and three qubit interaction<sup>193</sup> has been observed. Very recently, coherent manipulations have been achieved in this system in a setup which allows for simultaneous measurement<sup>108</sup>.

In the charge qubit case, a resonator coil between all qubits has been

proposed for a  $YY$  interaction<sup>30</sup>, which is tunable and of arbitrary range but does not appear to be compatible with parallel operation. Note, that a large coil usually provides strong coupling to external noise, but it can in principle be replaced by a large classical Josephson junction using the kinetic inductance<sup>194,195,196</sup>. Using the screening currents inside loop-shaped charge qubits, a tunable  $XX$  nearest-neighbor interaction can be implemented<sup>197</sup>. More easily, one can implement a capacitive interaction, which leads to  $ZZ$ . This is typically constant; however, using the capacitance of additional Josephson junctions it can be made tunable<sup>182</sup>. Coherent charge dynamics and conditional operations with constant capacitive interaction have been demonstrated<sup>79,107</sup>. A tunable nearest-neighbor  $XX + YY$  coupling is achieved by connection with SQUIDs; however, the interaction strength is rather low<sup>198</sup>. Charge qubits can profit from a cavity, mediating an  $XX$ - interaction<sup>199</sup> and nonclassical radiation<sup>200</sup>.

The interaction between qantronia can be implemented using a capacitor and is expected to be of  $XX + YY$  structure.

This variety of possible interactions opens the question, which type of interactions are efficient and about the importance of tunability, long range, and parallel operation. Clearly, tunability is not needed for the demonstration of gates on a few qubits similar to NMR<sup>201,10,107,202</sup>; however, with an increasing number of qubits, controls are supposed to become more and more complex. In fact, the in situ tunability of interactions is one of the main advantages of superconducting qubits and shouldnot be given up. On the other hand, long range interactions are less crucial as algorithms operate efficiently even on linear nearest neighbor arrays<sup>203</sup>. It is on the other hand absolutely crucial to operate in parallel.

## 9. Summary

Let's take an overview of the present status of superconducting Josephson qubits from a view point of the theme of this conference ; "Are the DiVincenzo criteria satisfied by today's experiments ?"

- (1) A scalable physical system of well-characterized qubits

Employing the very advanced micro and nano fabrication technology from the semiconductor industry, superconducting qubits have strong potential advantage in scalability towards the circuit level, including tunable coupling switches.

- (2) The ability to initialize the state of the qubits to a simple fiducial state

The requirement of proper initialization can be satisfied if superconducting qubit devices are operated at low enough temperature  $\sim 20$  mK, which is also far below the critical temperature of aluminum ( $\sim 1.2$  K), niobium ( $\sim 9$  K) or other superconducting materials, such that the ground state is occupied with probability nearly 1. The qubit state is protected from rapid energy relaxation once it is cooled below the critical temperature, because it is disconnected from the phonon bath and there is an energy gap in the quasi-particle density of states.

- (3) Long (relative) decoherence times, much longer than the gate-operation time

A typical decoherence time of a present superconducting Josephson qubit is  $T_2^* \approx 0.5 \mu\text{s}$  during free induction decay<sup>81,7,7</sup> and it reaches  $T_2 \approx 4 \mu\text{s}$  under the echo pulse technique<sup>91</sup>. Whereas a typical time for single qubit gate operation, e.g a  $\pi$ -rotation pulse, is an order of 0.1 ns under strong driving. The present few ns  $\pi$ -rotation time via the conditional side-band transition of qubit LC-resonator coupled system<sup>109,7</sup> is ready to improve as a design enabling strong driving. In order to demonstrate C-NOT gate operation, a series of phase-shifted composite side-band pulses are needed. So, the present typical decoherence time normalized by a single two-qubit gate operation time would be an order of  $10^3$ . This experimental value is a result at the optimal operating point, which is a commonly used strategy to decouple qubit to the first order from outside “charge” and “flux” noise<sup>81</sup>.

- (4) A universal set of quantum gates

An arbitrary rotational gate for a single qubit operation is realized by applying resonant microwave pulses from an on-chip microwave circuit. This is already demonstrated and established in all types of superconducting qubits, i.e., the “charge”<sup>77</sup>, “phase”<sup>69,70</sup>, “charge-phase”<sup>81,105</sup>, and “flux”<sup>75</sup> qubits. In order to achieve noise tolerant

qubit operation and to achieve two-axis qubit rotation without using slow detuning technique, NMR-like multi pulse sequence control has been demonstrated in a “charge-phase” qubit<sup>?</sup> and also in a “flux”<sup>95</sup> qubit respectively. The antiphase oscillation of the  $|01\rangle$  and  $|10\rangle$  states in the capacitively coupled Josephson phase two-qubits<sup>108</sup> has been observed. So far, the C-NOT gate operation has been demonstrated only in a “charge” two-qubit system<sup>107</sup>.

(5) A qubit-specific measurement capability

Measurement of qubit state can be done, for example, using an extremely sensitive magnetic flux quantum detector namely a SQUID which is placed adjacent to the qubit. Single-shot readout has been achieved in a “flux” qubit for the first time in the slow ramping readout method<sup>204,101</sup> and recently in a “charge” qubit using an S-SET pulsed readout technique<sup>103</sup> and very recently in a “charge-phase” qubit coupled to a transmission line resonator using reflection wave phase detection<sup>105</sup>. Furthermore, the state of the qubit can be measured by dispersive technique that probes the second derivative of the state energy with respect to qubit bias parameters. The phase degree of freedom is used to perform inductive readout<sup>106</sup> using Josephson bifurcation amplification<sup>?,?</sup>. This novel readout projects the state of the qubit typically in a few hundred nano second which is roughly two orders of magnitude faster than the conventional switching readout which inevitably includes the dead time due to a large numbers of generated quasiparticles to relax to the ground state. This new readout method has a lot of advantages with an improved signal to noise ratio and contrast. Thus the readout visibility of the coherent oscillation is becoming better approaching the unit visibility.

Certainly, theoretical proposals for meeting all DiVincenzo’s criteria have been put forward and no principal obstacle is known. However, a few experimental issues in decoherence, in particular the loss of visibility, are not fully understood today and may prove problematic if they are fundamental.

## Acknowledgments

We would like to thank Prof. M. Nakahara for organizing this fascinating conference and Kinki University for supporting it. We would like to thank all co-workers with whom we have obtained the results presented here. FKWs work is supported by ARDA through ARO contract No. P-43385-PH-QC and DFG through SFB 631.

## References

1. G. Moore, *Electronics* **38**, 114 (1965).
2. G. Moore, No Exponential is forever, Keynote Presentation International Solid State Circuits Conference, 2003.
3. I. Co., Expanding Moore's law, Available at [ftp://download.intel.com/labs/eml/download/EML\\_opportunity.pdf](ftp://download.intel.com/labs/eml/download/EML_opportunity.pdf) (2002).
4. M. Nielsen and I. Chuang, *Quantum Computation and Quantum Information* (Cambridge University Press, Cambridge, UK, 2000).
5. J. Preskill, Quantum computation lecture notes, Available at <http://www.theory.caltech.edu/people/preskill/ph219/>.
6. D. DiVincenzo, *Science* **270**, 255 (1995).
7. D. DiVincenzo, *Fortschr. Phys.* **48**, 771 (2000).
8. R. Hughes, the ARDA Quantum Information Science, and T. Panel, A Quantum Information Science and Technology Roadmap, available at <http://qist.lanl.gov>.
9. W. Kaminsky, S. Lloyd, and T. Orlando, quant-ph/0403090 (unpublished).
10. L. Vandersypen *et al.*, *Nature* **414**, 883 (2001).
11. N. Gershenfeld and I. Chuang, *Science* **275**, 350 (1997).
12. C. Monroe *et al.*, *Phys. Rev. Lett.* **75**, 4714 (1995).
13. J. Cirac and P. Zoller, *Phys. Rev. Lett.* **74**, 4091 (1995).
14. Q. Turchette *et al.*, *Phys. Rev. Lett.* **75**, 4710 (1995).
15. T. Pellizzari, S. Gardiner, J. Cirac, and P. Zoller, *Phys. Rev. Lett.* **75**, 3788 (1995).
16. E. Knill, R. Laflamme, and G. Milburn, *Nature* **409**, 46 (2001).
17. H.-J. Briegel *et al.*, *Journal of modern optics* **47**, 415 (2000).
18. D. Kielpinski, C. Monroe, and D. J. Wineland, *Nature* **417**, 709 (2002).
19. S. Sze, *Semiconductor devices, physics and technology* (Wiley-VCH, New York, 2001).
20. S. Thompson *et al.*, *Intel Technology Journal* **6**, (2002).
21. Y. Imry, *Introduction to Mesoscopic Physics* (Oxford University Press, Oxford, 1997).
22. *Mesoscopic electron transport*, No. E345 in *Proceedings of the NATO Advanced Study Institute*, edited by L. Kouwenhoven, G. Schön, and L. Sohn (Kluwer, Dordrecht, 1997).
23. A. Leggett, *Progr. Theor. Phys. Suppl.* **69**, 80 (1980).
24. A. Leggett and A. Garg, *Phys. Rev. Lett.* **54**, 857 (1985).

25. C. Tesche, Phys. Rev. Lett. **64**, 2358 (1990).
26. K. Likharev, Usp. Fiz. Nauk. **139**, 169 (1983).
27. P. Anderson, in *Lectures on the Many-Body Problem*, edited by E. Caianiello (Academic Press, New York, 1964), p. 113.
28. *Single Charge Tunneling*, No. B294 in *NATO ASI Series*, edited by H. Grabert and M. Devoret (Plenum, New York, 1992).
29. V. Bouchiat, D. V. et P. Joyez, D. Esteve, and M. Devoret, Physica Scripta **T76**, 165 (1998).
30. Y. Makhlin, G. Schön, and A. Shnirman, Rev. Mod. Phys. **73**, 357 (2001).
31. B. Kane, Nature **393**, 133 (1998).
32. D. Loss and D. DiVincenzo, Phys. Rev. A **57**, 120 (1998).
33. J. Elzerman *et al.*, Phys. Rev. B **67**, 161308 (2003).
34. R. Clark *et al.*, Los Alamos Science **27**, 284 (2002).
35. L. Vandersypen *et al.*, in *Quantum Computing and Quantum Bits in Mesoscopic Systems* (Kluwer, Dordrecht, 2002), Chap. 22.
36. G. Burkhard, H. Engel, and D. Loss, Fortschr. Physik **48**, 965 (2000).
37. R. Hanson *et al.*, Phys. Rev. Lett. **94**, 196802 (2005).
38. H. K. Onnes, Leiden Comm. **122b**, 124 (1911).
39. J. Bardeen, L. Cooper, and J. Schrieffer, Phys. Rev. **108**, 1175 (1957).
40. M. Tinkham, *Introduction to Superconductivity* (McGraw-Hill, New York, 1996).
41. P. de Gennes, *Superconductivity of metals and alloys* (Benjamin, N.Y., 1966).
42. J. Schrieffer, *Theory of Superconductivity* (Cummings, N.Y., 1988).
43. F. London, *Superfluids* (Wiley and Sons, N.Y., 1954).
44. R. Doll and M. Näbauer, Phys. Rev. Lett. **7**, 51 (1961).
45. L. Tian *et al.*, in *Quantum Mesoscopic Phenomena and Mesoscopic Devices in Microelectronics* (Kluwer, Dordrecht, 2000), Chap. Decoherence of the superconducting persistent current qubit, edited by I. O. Kulik and R. Ellialogulu.
46. L. Ioffe, V. Geshkenbein, C. Helm, and G. Blatter, Phys. Rev. Lett. **93**, 057001 (2004).
47. B. Josephson, Phys. Lett. **1**, 251 (1962).
48. A. Barone and G. Paterno, *Physics and applications of the Josephson effect* (Wiley, N.Y., 1982).
49. K. Likharev, *Dynamics of Josephson junctions and circuits* (Gordon and Breach, New York, 1986).
50. A. Golubov, M. Kupriyanov, and E. Il'ichev, Rev. Mod. Phys. **76**, 411 (2004).
51. R. Feynman, *Lectures in Physics* (Addison Wesley, New York, 1970), Vol. 3.
52. L. Landau and E. Lifshitz, *Statistical Physics 2* (Akademie-Verlag, Berlin, 1979).
53. S. Pereverzev *et al.*, Nature **388**, 449 (1997).
54. K. Sukhatme, Y. Mukharsky, T. Chui, and D. Pearson, Nature **411**, 280 (2001).
55. B. P. Anderson and M. A. Kasevich, Science **282**, 1686 (1998).

56. P. Hadley, private communication.
57. T. Orlando and K. Delin, *Foundations of applied superconductivity* (Prentice Hall, New York, 1991).
58. T. van Duzer and C. Turner, *Principles of superconductive devices and circuits* (Elsevier, Amsterdam, 1999).
59. V. Ambegaokar, U. Eckern, and G. Schön, Phys. Rev. Lett. **48**, 1745 (1982).
60. J. Clarke, in *Applications of Superconductivity* (Kluwer, Dordrecht, 2000), Chap. Low- and High-Tc SQUIDS and Some Applications, p. 1, edited by H. Weinstock.
61. J. Niemeyer, Supercond. Sci. and Technology **13**, 546 (2000).
62. J. von Delft and H. Schoeller, Ann. Phys. (Leipzig) **7**, 225 (1998).
63. A. Zaikin and G. Schön, Phys. Rep. **198**, 237 (1990).
64. H. van der Zant and R. Fazio, Phys. Rep. **355**, 236 (2001).
65. R. Feynman and F. Vernon, Ann. Phys. (N.Y.) **24**, 118 (1963).
66. G. Ingold, in *Quantum transport and dissipation* (Wiley-VCH, Weinheim, 1998), Chap. Dissipative quantum systems.
67. A. Caldeira and A. Leggett, Phys. Rev. Lett. **46**, 211 (1981).
68. A. Caldeira and A. Leggett, Ann. Phys. (NY) **149**, 374 (1983).
69. J. Martinis, S. Nam, J. Aumentado, and C. Urbina, Phys. Rev. Lett **89**, 117907 (2002).
70. Y. Yu *et al.*, Science **286**, 889 (2002).
71. A. Berkley *et al.*, Science **300**, 1548 (2003).
72. J. Friedman *et al.*, Nature **46**, 43 (2000).
73. J. Mooij *et al.*, Science **285**, 1036 (1999).
74. T. P. Orlando *et al.*, Phys. Rev. B **60**, 15398 (1999).
75. I. Chiorescu, Y. Nakamura, C. Harmans, and J. Mooij, Science **299**, 1869 (2003).
76. E. Il'ichev *et al.*, Phys. Rev. Lett. **91**, 097906 (2003).
77. Y. Nakamura, Y. Pashkin, and J. Tsai, Nature **398**, 786 (1999).
78. Y. Nakamura, Y. A. Pashkin, T. Yamamoto, and J. S. Tsai, Phys. Rev. Lett. **88**, 047901 (2002).
79. Y. Pashkin *et al.*, Nature **421**, 823 (2003).
80. K. Lehnert *et al.*, Phys. Rev. Lett. **90**, 027002 (2003).
81. D. Vion *et al.*, Science **296**, 286 (2002).
82. L. B. Ioffe *et al.*, Nature **398**, 679 (1999).
83. A. Blais and A. Zagoskin, Phys. Rev. A **61**, 042308 (2000).
84. L. B. Ioffe *et al.*, Nature **398**, 678 (2002).
85. G. J. Dolan, Appl. Phys. Lett. **31**, 3 (1977).
86. A. Leggett, J. Phys. C **14**, 415 (2002).
87. W. Dür, C. Simon, and J. Cirac, Phys. Rev. Lett. **89**, 210402 (2002).
88. D. Crankshaw and T. Orlando, IEEE Trans. Appl. Supercond. **11**, 1006 (2001).
89. A. van den Brink, Phys. Rev. B **71**, 064503 (2005).
90. G. Burkard *et al.*, Phys. Rev. B **71**, 134504 (2005).
91. P. Bertet *et al.*, cond-mat/0412485 (unpublished).
92. A. Leggett *et al.*, Rev. Mod. Phys. **59**, 1 (1987).

93. Y. Nakamura, Y. Pashkin, and J. Tsai, *Phys. Rev. Lett.* **87**, 246601 (2001).
94. J. Clarke *et al.*, *Science* **239**, 992 (1988).
95. T. Kutsuzawa *et al.*, cond-mat/0501592 (unpublished).
96. R. Simmonds *et al.*, *Phys. Rev. Lett.* **93**, 077003 (2004).
97. K. B. Cooper *et al.*, *Phys. Rev. Lett.* **93**, 180401 (2004).
98. T. Bauch *et al.*, *Phys. Rev. Lett.* **94**, 087003 (2005).
99. K. Inomata *et al.*, cond-mat/040412604 (unpublished).
100. K. Ueda *et al.*, *Appl. Phys. Lett.* **86**, 172502 (2005).
101. H. Tanaka *et al.*, cond-mat/0407299 (unpublished).
102. H. Nakano *et al.*, cond-mat/0406622 (unpublished).
103. O. Astafiev *et al.*, *Phys. Rev. B* **69**, 180507(R) (2004).
104. P. Bertet *et al.*, *Phys. Rev. B* **70**, 100501(R) (2004).
105. A. Wallraff *et al.* (unpublished).
106. A. Lupascu *et al.*, *Phys. Rev. Lett.* **93**, 177006 (2004).
107. T. Yamamoto *et al.*, *Nature* **425**, 941 (2003).
108. R. McDermott *et al.*, *Science* **307**, 1299 (2005).
109. I. Chiorescu *et al.*, *Nature* **431**, 159 (2004).
110. A. Wallraff *et al.*, *Nature* **431**, 162 (2004).
111. E. Hecht, *Optics* (Addison-Wesley, Reading, Mass., 1987).
112. A. Peres, *Quantum Theory: Concept and Methods* (Kluwer, Dordrecht, 1993).
113. D. Giulini *et al.*, *Decoherence and the Appearance of a Classical World in Quantum Theory* (Springer, Heidelberg, 1996).
114. W. Unruh, *Phys. Rev. D* **40**, 1053 (1989).
115. C. Cohen-Tannoudji, J. Dupont-Roc, and G. Grynberg, *Atom-Photon Interactions* (Wiley Interscience, New York, 1998).
116. E. Schrödinger, *Naturwissenschaften* **23**, 807, 823, 844 (1935).
117. V. Emery and A. Luther, *Phys. Rev. B* **9**, 215 (1974).
118. P. Anderson, *Phys. Rev. Lett.* **18**, 1049 (67).
119. R. J. Schoelkopf *et al.*, in *Quantum Noise, Nato ASI* (Kluwer, Dordrecht, 2002), Chap. Qubits as spectrometers of quantum noise, edited by Yu.V. Nazarov and Ya.M. Blanter.
120. R. Aguado and L. Kouwenhoven, *Phys. Rev. Lett.* **84**, 1986 (2000).
121. A. Cottet, Ph.D. thesis, Universite Paris 6, 2002.
122. J. Martinis *et al.*, *Phys. Rev. B* **67**, 094510 (2003).
123. C. Slichter, *Principles of magnetic resonance*, No. 1 in *Springer Series in Solid-State Sciences* (Springer, Berlin, 1996).
124. M. Grifoni, E. Paladino, and U. Weiss, *Eur. Phys. J B* **10**, 719 (1999).
125. L. Tian, S. Lloyd, and T. Orlando, *Phys. Rev. B* **65**, 144516 (2002).
126. A. Garg, J. Onuchic, and V. Ambegaokar, *J. Chem. Phys.* **83**, 4491 (1985).
127. A. Abragam, *Principles of nuclear magnetism*, Vol. 32 of *International series of monographs on physics* (Clarendon Press, Oxford, 1983).
128. S. Adler, *Studies in history and philosophy of modern physics* **34**, 135 (2003).
129. S. Nakaijma, *Progr. Theor. Phys.* **20**, 948 (1958).
130. R. Zwanzig, *Phys. Rev.* **124**, 983 (1961).

131. P. Argyres and P. Kelley, Phys. Rev. **134**, A98 (1964).
132. U. Weiss, *Quantum Dissipative Systems*, No. 10 in *Series in modern condensed matter physics*, 2 ed. (World Scientific, Singapore, 1999).
133. H. Spohn, Rev. Mod. Phys. **52**, 569 (1980).
134. G. Lindblad, Commun. Math. Phys. **48**, 119 (1976).
135. R. Alicki and K. Lendi, *Quantum dynamical semigroups and applications*, No. 286 in *Lecture notes in physics* (Springer, Berlin, 1976).
136. H. Carmichael, *An open systems approach to quantum optics* (Springer, Berlin, 1993).
137. C. Gardiner and P. Zoller, *Quantum Noise. A Handbook of Markovian and Non-Markovian Quantum Stochastic Methods with Applications to Quantum Optics*, *Springer series in synergetics* (Springer, Berlin, 1999).
138. D. Loss and D. DiVincenzo, cond-mat/0304118 (unpublished).
139. F. Bloch, Phys. Rev. **105**, 1206 (1957).
140. A. Redfield, IBM J Res. Develop. **1**, 19 (1957).
141. M. Plenio and P. Knight, Rev. Mod. Phys. **70**, 101 (1998).
142. J. Dalibard, Y. Castin, and K. Molmer, Phys. Rev. Lett. **68**, 580 (1992).
143. A. Korotkov, Phys. Rev. B **67**, 235408 (2003).
144. T. Costi, Phys. Rev. Lett. **80**, 1038 (1998).
145. S. Kehrein and A. Mielke, J. Stat. Phys. **90**, 889 (1998).
146. M. Keil and H. Schoeller, Phys. Rev. B **63**, 180302 (2001).
147. A. Leggett, Phys. Rev. B **30**, 1208 (1984).
148. C. van der Wal, F. Wilhelm, C. Harmans, and J. Mooij, Eur. Phys. J. B **31**, 111 (2003).
149. T. Robertson *et al.*, Phys. Rev. B **72**, 024513 (2005).
150. F. K. Wilhelm, Phys. Rev. B **68**, 060503(R) (2003).
151. S. K. and S. Kehrein and J. von Delft, Phys. Rev. B **70**, 014516 (2004).
152. F. Wilhelm, S. Kleff, and J. van Delft, Chem. Phys. **296**, 345 (2004).
153. M. Thorwart, E. Paladino, and M. Grifoni, Chem. Phys. **296**, 333 (2004).
154. M. Goorden, M. Thorwart, and M. Grifoni, Phys. Rev. Lett. **93**, 267005 (2004).
155. A. Shnirman and G. Schoen, Phys. Rev. Lett. **57**, 15400 (1998).
156. C. van der Wal *et al.*, Science **290**, 773 (2000).
157. P. Joyez *et al.*, Journal of superconductivity **12**, 757 (1999).
158. W. Coffey, Y. Kalmykov, and J. Waldron, *The Langevin equation: With applications in physics chemistry and electrical engineering*, No. 11 in *Series in contemporary chemical physics* (World Scientific, Singapore, 1996).
159. N. Prokovev and P. Stamp, Rep. Prog. Phys. **63**, 669 (2000).
160. H. Gassmann, F. Marquardt, and C. Bruder, Phys. Rev. E **66**, 041111 (02).
161. E. Paladino, L. Faoro, G. Falci, and R. Fazio, Phys. Rev. Lett. **88**, 228304 (2002).
162. K. Rabenstein, V. Sverdlov, and D. Averin, JETP Lett. **79**, 646 (2004).
163. Y. Galperin, B. Altshuler, and D. Shantsev, in *Fundamental problems of mesoscopic physics: Interaction and decoherence*, *NATO-ASI* (Plenum, New York, 2003), Chap. Low-frequency noise as a source of dephasing a qubit.
164. A. Shnirman, Y. Makhlin, and G. Schön, Phys. Scr. **T102**, 147 (2002).

165. P. Dutta and P. Horn, *Rev. Mod. Phys.* **53**, 497 (1981).
166. R. Wakai and D. van Harlingen, *Phys. Rev. Lett.* **58**, 1687 (1987).
167. N. Zimmermann, J. Cobb, and A. Clark, *Phys. Rev. B* **56**, 7675 (1997).
168. M. Weissman, *Rev. Mod. Phys.* **60**, 537 (1988).
169. N. van Kampen, *Stochastic processes in physics and chemistry* (Elsevier, Amsterdam, 1997).
170. L. Arnold, *Stochastische Differentialgleichungen* (Oldenbourg, Munich, 1973).
171. L. Viola and S. Lloyd, *Phys. Rev. A* **58**, 2733 (1998).
172. L. Viola, E. Knill, and S. Lloyd, *Phys. Rev. Lett.* **82**, 2417 (1999).
173. L. Viola, S. Lloyd, and E. Knill, *Phys. Rev. Lett.* **83**, 4888 (1999).
174. H. Carr and E. Purcell, *Phys. Rev.* **94**, 630 (1954).
175. H. Gutmann, F. Wilhelm, W. Kaminsky, and S. Lloyd, *Quant. Inf. Proc.* **3**, 247 (2004).
176. G. Weiss, *Aspects and Applications of the Random Walk* (North-Holland, Amsterdam, 1994).
177. H. Gutmann, W. Kaminsky, S. Lloyd, and F. Wilhelm, *Phys. Rev. A* **71**, 020302(R) (2005).
178. L. Faoro and L. Viola, *Phys. Rev. Lett.* **92**, 117905 (2004).
179. G. Falci, A. D'Arrigo, A. Mastellone, and E. Paladino, *Phys. Rev. A* **70**, R40101 (2004).
180. J. Majer *et al.*, *Phys. Rev. Lett.* **94**, 090501 (2005).
181. F. Strauch *et al.*, *Phys. Rev. Lett.* **91**, 167005 (2003).
182. D. Averin and C. Bruder, *Phys. Rev. Lett.* **91**, 057003 (2003).
183. J. Clarke *et al.*, *Phys. Scr.* **T102**, 173 (2002).
184. C. Hilbert and J. Clarke, *J. Low Temp. Phys.* **61**, 237 (1985).
185. A. Barenco, D. Deutsch, A. Ekert, and R. Josza, *Phys. Rev. Lett.* **74**, 4083 (1995).
186. J. Zhang, J. Vala, S. Sastry, and K. Whaley, *Phys. Rev. A* **67**, 042313 (2003).
187. Y. Makhlin, *Quant. Inf. Proc.* **1**, 243 (2002).
188. J. You, Y. Nakamura, and F. Nori, *Phys. Rev. B* **71**, 0242532 (2005).
189. M. Storz and F. Wilhelm, *Appl. Phys. Lett.* **83**, 2389 (2003).
190. L. Levitov, T. Orlando, J. Majer, and J. Mooij, cond-mat/0108266 (unpublished).
191. P. Johnson *et al.*, *Phys. Rev. B* **67**, 020509 (2002).
192. A. Berkley *et al.*, *Science* **300**, 1548 (2003).
193. H. Xu *et al.*, *Phys. Rev. Lett.* **94**, 027003 (2005).
194. J. You, J. Tsai, and F. Nori, *Phys. Rev. Lett.* **89**, 197902 (2002).
195. L. Wei, Y. x. Liu, and F. Nori, *Europhys. Lett.* **67**, 1004 (2004).
196. L. Wei, Y. x. Liu, and F. Nori, *Phys. Rev. B* **71**, 134506 (2005).
197. J. Lantz, M. Wallquist, V. Shumeiko, and G. Wendin, *Phys. Rev. B* **70**, 140507(R) (2004).
198. J. Siewert, R. Fazio, G. Palma, and E. Sciacca, *J. Low Temp. Phys.* **118**, 795 (2000).
199. Y. x. Liu, L. Wei, and F. Nori, *Phys. Rev. A* **71**, 063820 (2005).

200. M. Paternostro, G. Falci, M. Kim, and G. Palma, Phys. Rev. B **69**, 214502 (2004).
201. A. Spoerl *et al.*, quant-ph/0504202 (unpublished).
202. C. Rigetti, A. Blais, and M. Devoret, Phys. Rev. Lett. **94**, 240502 (2005).
203. A. Fowler, S. Devitt, and L. Hollenberg, Quant. Inf. Comp. **4**, 237 (2004).
204. H. Tanaka, Y. Sekine, S. Saito, and H. Takayanagi, Physica C **368**, 300 (2002).